The Astrophysical Journal, 878:42 (18pp), 2019 June 10 https://doi.org/10.3847/1538-4357/ab1eac

Elemental Abundances in M31: Alpha and Iron Element Abundances from Low-resolution Resolved Stellar Spectroscopy in the Stellar Halo

Ivanna Escala[1,2], Evan N. Kirby[1], Karoline M. Gilbert[3,4], Emily C. Cunningham[5], and Jennifer Wojno[4]
[1] Department of Astronomy, California Institute of Technology, 1200 E California Blvd., Pasadena, CA, 91125, USA; ie@astro.caltech.edu
[2] Department of Astrophysical Sciences, Princeton University, 4 Ivy Ln., Princeton, NJ 08540, USA
[3] Space Telescope Science Institute, 3700 San Martin Dr., Baltimore, MD 21218, USA
[4] Department of Physics & Astronomy, Bloomberg Center for Physics and Astronomy, John Hopkins University, 3400 N. Charles St., Baltimore, MD 21218, USA
[5] Department of Astronomy and Astrophysics, University of California, Santa Cruz, 1156 High St., Santa Cruz, CA, 95064, USA
Received 2018 November 15; revised 2019 April 9; accepted 2019 April 30; published 2019 June 12

Abstract

Measurements of [Fe/H] and [α/Fe] can probe the minor merging history of a galaxy, providing a direct way to test the hierarchical assembly paradigm. While measurements of [α/Fe] have been made in the stellar halo of the Milky Way (MW), little is known about detailed chemical abundances in the stellar halo of M31. To make progress with existing telescopes, we apply spectral synthesis to low-resolution DEIMOS spectroscopy ($R \sim 2500$ at 7000 Å) across a wide spectral range (4500 Å $< \lambda <$ 9100 Å). By applying our technique to low-resolution spectra of 170 giant stars in five MW globular clusters, we demonstrate that our technique reproduces previous measurements from higher resolution spectroscopy. Based on the intrinsic dispersion in [Fe/H] and [α/Fe] of individual stars in our combined cluster sample, we estimate systematic uncertainties of ∼0.11 dex and ∼0.09 dex in [Fe/H] and [α/Fe], respectively. We apply our method to deep, low-resolution spectra of 11 red giant branch stars in the smooth halo of M31, resulting in higher signal-to-noise ratios per spectral resolution element compared to DEIMOS medium-resolution spectroscopy, given the same exposure time and conditions. We find $\langle$[α/Fe]$\rangle = 0.49 \pm 0.29$ dex and $\langle$[Fe/H]$\rangle = -1.59 \pm 0.56$ dex for our sample. This implies that—much like the MW—the smooth halo field of M31 is likely composed of disrupted dwarf galaxies with truncated star formation histories that were accreted early in the halo's formation.

Key words: galaxies: abundances – galaxies: formation – galaxies: halos – Local Group – stars: abundances

1. Introduction

Stellar chemical abundances are a key component in determining the origins of stellar halos of Milky Way (MW)-like galaxies, providing insight into the formation of galaxy-scale structure. The long dynamical times of stellar halos allow tidal features to remain identifiable in phase space, in terms of kinematics and chemical abundances, for gigayear timescales. Stellar chemical abundances of stars retain information about the star formation history (SFH) and accretion times of progenitor satellite galaxies, even when substructures can no longer be detected by kinematics alone. In particular, measurements of metallicity[6] and α-element abundances provide a way of directly testing the hierarchical assembly paradigm central to ΛCDM cosmology, providing a fossil record of the formation environment of stars accreted onto the halo.

The [α/Fe] ratio serves as a useful diagnostic of formation history, given that it traces the star formation timescales of a galaxy (e.g., Gilmore & Wyse 1998). Type II supernovae (SNe II) produce abundant α-elements (O, Ne, Mg, Si, S, Ar, Ca, and Ti), increasing [α/Fe], whereas SNe Ia produce Fe-rich ejecta, reducing [α/Fe]. While measurements of [α/Fe] have been made in the stellar halo of the MW, little is known about the detailed chemical abundances of the stellar halo of M31. A comparable understanding of the properties of the MW and M31 stellar halos is required to verify basic assumptions about how the MW evolved, where such assumptions are used to extrapolate MW-based results to studies of galaxies beyond the Local Group.

Although high-resolution ($R \gtrsim 15{,}000$), high signal-to-noise ratio (S/N) spectra enables simultaneous measurements of a star's temperature, surface gravity, and individual element abundances based on individual lines, it is impractical to achieve high-enough S/N for traditional high-resolution spectroscopic abundance analysis (e.g., Kirby & Cohen 2012) for red giant branch (RGB) stars at the distance of M31 (783 kpc; Stanek & Garnavich 1998).

It is possible to obtain spectroscopic metallicity measurements of M31 RGB stars from medium-resolution spectra (MRS; $R \sim 6000$) using spectral synthesis (e.g., Kirby et al. 2008a). This method leverages the entire spectrum's metallicity information simultaneously, enabling measurements of abundances from relatively low-S/N spectra. Kirby et al. (2008b, 2010, 2013) successfully measured [Fe/H] and [α/Fe] in MW globular clusters (GCs), MW dwarf spheroidal (dSph) satellite galaxies, and Local Group dwarf irregular galaxies, showing that abundances can be measured to a precision of ∼0.2 dex from spectra with S/N ∼ 15 Å^{-1}.

It was only in 2014 that spectral synthesis was applied to individual RGB stars in the M31 system for the first time (Vargas et al. 2014a, 2014b). Existing spectroscopic chemical abundance measurements in M31 are primarily based on metallicity estimates from the strength of the calcium triplet (Chapman et al. 2006; Koch et al. 2008; Kalirai et al. 2009;

[6] We define metallicity in terms of stellar iron abundance, [Fe/H], where [Fe/H] = $\log_{10}(n_{Fe}/n_H) - \log_{10}(n_{Fe}/n_H)_\odot$.

Richardson et al. 2009; Tanaka et al. 2010; Gilbert et al. 2014; Ibata et al. 2014; Ho et al. 2015). Vargas et al. (2014a) measured [α/Fe] and [Fe/H] for a total of 226 red giants in nine M31 satellite galaxies. Although Vargas et al. (2014a) measured [α/Fe] for nine M31 dSphs, only a single dSph, And V, shows a clear chemical abundance pattern, where [α/Fe] declines with [Fe/H]. However, the present spectroscopic sample size and measurement uncertainties of the And V data enable only qualitative conclusions about the chemical evolution of the dSph. Obtaining more quantitative descriptions of the chemical enrichment and SFHs of the M31 system requires higher S/N spectroscopic data, which results in smaller uncertainties on abundance measurements. Only then can one-zone numerical chemical evolution models (Lanfranchi & Matteucci 2003, 2007, 2010; Lanfranchi et al. 2006; Kirby et al. 2011b) be reliably applied to measurements to derive star formation and mass assembly histories.

Although Vargas et al. (2014a, 2014b) demonstrated the feasibility of measuring [Fe/H] and [α/Fe] at the distance of M31, measuring [Fe/H] and [α/Fe] more precisely requires deep ($\sim$6 hr) observations with DEIMOS using the 600 line mm^{-1} grating to yield higher S/N for the same exposure time and observing conditions. For magnitudes fainter than $I_0 \sim 21$ (0.5 mag below the tip of M31's RGB), sky line subtraction at $\lambda > 7000$ Å becomes the dominant source of noise in DEIMOS spectra observed with the 1200 line mm^{-1} grating. Given the access to blue optical wavelengths granted by the 600 line mm^{-1} grating, its spectra are less susceptible to the effects of sky noise. Additionally, using the 600 line mm^{-1} grating achieves higher S/N per pixel for stars as faint as $I_0 \sim 21.8$.

Although using the 600 line mm^{-1} grating with DEIMOS results in a gain in S/N and wavelength coverage, it corresponds to a decrease in spectral resolution ($\sim$2.8 Å FWHM, or $R \sim 2500$ at 7000 Å, compared to $\sim$1.3 Å and $R \sim 5400$ for the 1200 line mm^{-1} grating). Increasing the spectral range compensates for the decrease in spectral resolution, given the increase in the amount of available abundance information contained in the spectrum resulting from the higher density of absorption features at bluer optical wavelengths.

In this paper, we expand upon the technique first presented by Kirby et al. (2008a), applying spectral synthesis to low-resolution spectroscopy (LRS; $R \sim 2500$) across a wide spectral range ($\lambda \sim$ 4500–9100 Å). In Section 2, we describe our data reduction and GC observations. Sections 3 and 4 detail our preparations of the observed spectrum and the subsequent abundance analysis. This includes a presentation of our new line list and grid of synthetic spectra. In Section 5, we illustrate the efficacy of our technique applied to MW GCs and compare our results to chemical abundances from high-resolution spectroscopy (HRS) in Section 6. We quantify the associated systematic uncertainties in Section 7. We conclude by measuring [α/Fe] and [Fe/H] in an M31 stellar halo field in Section 8 and summarize in Section 9.

2. Observations

We utilize observations of Galactic GCs, MW dwarf spheroidal (dSph) galaxies, and MW halo stars (Table 1) taken using Keck/DEIMOS (Faber et al. 2003) to validate our LRS method of spectral synthesis. For our science configuration (for all observations, including M31 observations; Section 8.1), we used the GG455 filter with a central wavelength of 7200 Å, in combination with the 600ZD grating and 0.″7 slit widths. When targeting individual stars, such as the MW halo stars in Table 1, we utilized the long slit, as opposed to a slitmask intended to target multiple stars simultaneously.

The spectral resolution for the 600 line mm^{-1} grating is approximately $\sim$2.8 Å FWHM, compared to $\sim$1.3 Å FWHM for the 1200 line mm^{-1} grating used in prior observations (Kirby et al. 2010, 2013). The wavelength range for each spectrum obtained with the 600ZD grating is within 4100 Å^{-1} μm, where we generally omit $\lambda \lesssim 4500$ Å, owing to poor S/N in this regime and the presence of the *G* band. We also omit $\lambda > 9100$ Å, which extends beyond the wavelength coverage of our grid of synthetic spectra (Section 4.2).

To extract one-dimensional spectra from the raw DEIMOS data, we used a modification of version 1.1.4 of the data reduction pipeline developed by the DEEP2 Galaxy Redshift Survey (Cooper et al. 2012; Newman et al. 2013). Guhathakurta et al. (2006) provides a detailed description of the data reduction process. Modifications to the software include those of Simon & Geha (2007), where the pipeline was repurposed for bright unresolved stellar sources (as opposed to faint, resolved galaxies). In addition, we include custom modifications to correct for atmospheric refraction in the two-dimensional raw spectra, which affects bluer optical wavelengths, and to identify lines in separate arc lamp spectra, as opposed to a single stacked arc lamp spectrum.

3. Preparing the Spectrum for Abundance Measurement

3.1. Telluric Absorption Correction

Unlike the red side of the optical (6300–9100 Å), there is no strong telluric absorption in the bluer regions (4500–6300 Å). As such, we do not make any corrections to the observed stellar spectra to take into account absorption from Earth's atmosphere in this wavelength range.

For the red (6100–9100 Å), we correct for the absorption of Earth's atmosphere using the procedure described in Kirby et al. (2008a). We adopt HD 066665 (B1V), observed on 2012 April 23 with an airmass of 1.081, using a long slit in the same science configuration (Section 2) as our data, as our spectrophotometric standard.

3.2. Spectral Resolution Determination

In contrast to Kirby et al. (2008a), who determined the spectral resolution as a function of wavelength based on the Gaussian widths of hundreds of sky lines, we assume a constant resolution, expressed as the typical FWHM of an absorption line, across the entire observed spectrum ($\sim$4500–9100 Å). Owing to the dearth of sky lines at bluer wavelengths, the number of available sky lines is insufficient to reliably determine the resolution as a function of wavelength. As an alternative, we introduce an additional parameter, $\Delta\lambda$, or the spectral resolution, into our chi-squared minimization, which determines the best-fit synthetic spectrum for each observed spectrum (Section 4.5).

3.3. Continuum Normalization

It is necessary to normalize the observed flux by its slowly varying stellar continuum in order to meaningfully compare to synthetic spectra for the abundance determination (Section 4.5). To obtain reliable abundances from spectral synthesis of low- and medium-resolution spectra dominated by

Table 1
MW and dSph DEIMOS Observations

Object	Slitmask	α_{J2000}	δ_{J2000}	Date	Seeing ($''$)	Airmass	t_{exp}[a] (s)	N_{target}	N_{member}[b]
MW Globular Clusters									
NGC 2419	n2419c	07:38:09.67	+38:51:15.0	2015 Oct 9	0.6	1.23	2 × 1380	92	61
NGC 1904 (M79)	1904l2	05:24:15.37	−24:31:31.3	2015 Oct 8	0.8	1.40	2 × 1260	96	18
NGC 6864 (M75)	n6864a	20:06:14.03	−21:55:16.4	2015 May 19	0.9	1.56	3 × 1080	86	35
NGC 6341 (M92)	n6341b	17:17:23.68	+43:06:49.4	2018 Oct 11	0.6	1.52	6 × 300	146	33
NGC 7078 (M15)	7078l1	21:29:48.03	+12:10:23.0	2015 May 19	0.9	1.16	2 × 1140	169	48
dSphs									
Draco	dra11	17:19:46.87	+57:57:21.1	2019 Mar 10	1.6	1.39	4280	138	⋯
Canes Venatici I	CVnIa	13:28:02.47	+33:32:49.5	2018 May 20	1.0	1.3	6 × 1200	122	⋯
Ursa Minor	bumib	15:09:28.75	+67:13:07.1	2018 May 20	1.0	1.68	7 × 1200	124	⋯
MW Halo									
HD 20512	LVMslitC	03:18:27.14	+15:10:38.29	2019 Mar 10	1.2	1.35	10	⋯	⋯
HD 21581	LVMslitC	03:28:54.48	−00:25:03.10	2019 Mar 10	1.2	1.45	171	⋯	⋯
HD 88609	LVMslitC	10:14:28.98	+53:33:39.34	2019 Mar 10	1.2	1.43	44	⋯	⋯
SAO 134948	LVMslitC	06:46:03.69	+67:13:45.75	2019 Mar 10	1.2	1.49	180	⋯	⋯
BD +80245	LVMslitC	08:11:06.23	+79:54:29.55	2019 Mar 10	1.2	1.99	3 × 300	⋯	⋯

Notes.
[a] In the case of multiple exposures with unequal exposure times, we indicate the total exposure time.
[b] Number of RGB and AGB members (Kirby et al. 2016) per slitmask. For dSph slitmasks, we do not fully evaluate membership because we utilized these observations only for comparison to the HRS literature (Section 6).

weak absorption features, the continuum determination must be accurate (Kirby et al. 2009; Shetrone et al. 2009). This is particularly important for bluer wavelengths, where absorption lines are so numerous and dense that we cannot define "continuum regions" (Kirby et al. 2008a) in the blue. Instead, we utilize the entire observed spectrum, excluding regions with strong telluric absorption and bad pixels, to determine the continuum for 4500–9100 Å. In contrast to Kirby et al. (2008a), we do not utilize continuum regions at redder wavelengths (6300–9100 Å), despite the fact that they can be reliably defined, to maintain consistency in the continuum normalization method between each wavelength region of the observed spectrum.

We determined the initial continuum fit to the raw observed spectrum, which we shift into the rest frame, using a third-order B-spline with a breakpoint spacing of 200 pixels, excluding 5 pixels around the chip gap and at the start and stop wavelengths of the observed spectrum. In all steps, we weighted the spline fit by the inverse variance of each pixel in the observed spectrum. We performed sigma clipping, such that pixels that deviate by more than 5σ (0.1σ) above (below) the fit are excluded from the subsequent continuum determination, where σ is the inverse square root of the inverse variance array. We did not perform the fit iteratively beyond the above steps, given that our stringent criterion to prevent the numerous absorption lines from offsetting our continuum determination can eliminate a significant fraction of the pixels from subsequent iterations of the fit.

To further refine our continuum determination, we recalculate the continuum fit iteratively in the initial step of the abundance analysis (Section 4.5). Once we have found a best-fit synthetic spectrum, we divide the continuum-normalized observed spectrum by the best-fit synthetic spectrum to construct a "flat noise" spectrum, which captures the higher order terms in the observed spectrum not represented in the fit. We fit a third-order B-spline with a breakpoint spacing of 100 pixels to the flat noise spectrum, excluding 3σ deviant (above and below the fit) pixels, dividing the continuum-normalized observed spectrum by this fit. The modified continuum-normalized spectrum is then used in the next iteration of the continuum refinement until convergence is achieved (Section 4.5).

Table 2
Spectral Features (4100–6300 Å)

Feature	Wavelength(s) (Å)
Hδ	4101.734
Ca I	4226.730
G band (CH absorption)	4300–4315
Hγ	4340.462 (4335–4345)[a]
Hβ	4861.35 (4856–4866)
Mg I (b4)	5167.322
Mg I (b2)	5172.684
Mg I (b1)	5183.604
Mg H	4845, 5622
Na D1,D2	5895.924, 5889.951 (5885–5905)

Note.
[a] Wavelength regions indicated in parentheses indicate regions that are omitted from the spectral fit.

3.4. Pixel Masks

In addition to wavelength masks corresponding to a particular abundance (Section 4.4), we constructed a pixel mask for each analyzed observed spectrum. Typically excluded regions include 5 pixels on either side of the chip gap between the blue and red sides of the CCD, areas with improper sky line subtraction, the region around the Na D1 and D2 lines (5585–5905 Å), and other apparent instrumental artifacts. Table 2 includes a summary of prominent spectral features in DEIMOS spectra between 4100 and 6300 Å, where wavelength

ranges given in parentheses indicate regions that are masked. For example, we excluded 10 Å regions around Hγ (4335–4345 Å) and Hβ (4856–4866 Å). Given that MOOG (Sneden 1973), the spectral synthesis software utilized to generate our grid of synthetic spectra (Section 4.2, does not incorporate the effects of nonlocal thermodynamic equilibrium, it cannot properly model the strong Balmer lines. If necessary, we also masked regions where the initial continuum fit failed, most often owing to degrading S/N as a function of wavelength at bluer wavelengths ($\lesssim$4500 Å). As for the red (6300–9100 Å), we adopted the pixel mask from Kirby et al. (2008a), which excludes spectral features such as the Ca II triplet, Hα, and regions with strong telluric absorption.

3.5. Signal-to-noise Estimation

We estimate the S/N per angstrom for objects observed with the 600 line mm^{-1} grating from wavelength regions of the spectrum utilized in the initial continuum determination (Section 3.3). Given that we cannot define continuum regions for wavelengths blueward of 6300 Å, we calculate the S/N after the continuum refinement process (Section 4.5). We estimate the noise as the deviation between the continuum-refined observed spectrum and the best-fit synthetic spectrum and the signal as the best-fit synthetic spectrum itself. The S/N estimate per pixel is the median of the S/N as a function of wavelength calculated from these quantities, where we exclude pixels that exceed the average noise threshold by more than 3σ. To convert to units of per angstrom, we multiply this quantity by the inverse square root of the pixel scale (∼0.64 Å for the 600 line mm^{-1} grating).

4. Chemical Abundance Analysis

Here, we present a new library of synthetic spectra in the range of 4100–6300 Å. In this section, we describe our procedure for spectral synthesis in the blue, where we use our new grid in conjunction with the red grid of Kirby et al. (2008a) to measure abundances across an expanded optical range (4100–9100 Å).

4.1. Line List

We constructed a line list of wavelengths, excitation potentials (EPs), and oscillator strengths ($\log gf$) for atomic and molecular transitions in the spectral range covering 4100–6300 Å for stars in our stellar parameter range ($T_{\rm eff} > 4000$ K). We queried the Vienna Atomic Line Database (Kupka et al. 1999) and the National Institute of Standards and Technology (NIST) Atomic Spectra Database (Kramida et al. 2016) for all transitions of neutral or singly ionized atoms with EP < 10 eV and $\log gf > -5$, supplementing the line list with molecular (Kurucz 1992) and hyperfine transitions (Kurucz 1993). All Fe I line oscillator strengths from Fuhr & Wiese (2006) are included in the NIST database.

Next, we compared synthetic spectra (Section 4.2) of the Sun and Arcturus, generated from our line list and model stellar atmospheres, to high-resolution spectra (Hinkle et al. 2000) of the respective stars. We adopted $T_{\rm eff} = 5780$ K, $\log g = 4.44$ dex, [Fe/H] = 0 dex, and [α/Fe] = 0 dex for the Sun. For Arcturus, we adopted $T_{\rm eff} = 4300$ K, $\log g = 1.50$ dex, and [Fe/H] = −0.50 dex, and [α/Fe] = 0 dex (Peterson et al. 1993).

To produce agreement between the synthetic and observed spectra, we vetted the line list by manually adjusting the oscillator strengths of aberrant atomic lines as necessary. We preferred the Sun over Arcturus in this process, given that Arcturus is a cool K-giant star with stronger molecular absorption features (e.g., the *G* band) that are more difficult to match. For features absent from the line list, which could not be resolved by considering lines with $\log gf < -5$, we included Fe I transitions with EPs and $\log gf$ to match the observed strength in both the Sun and Arcturus. We present the final blue line list in a format compatible with MOOG in Table 3. The line list contains 132 chemical species (atomic, molecular, neutral, and ionized), including 74 unique elements and two molecules (CN and CH). In total, the line list contains 53,164 atomic line transitions and 58,062 molecular transitions.

Figure 1 illustrates a comparison between the Hinkle spectra and their syntheses for the Sun and Arcturus. At the expected resolution of the DEIMOS 600ZD grating (∼2.8 Å), the mean absolute deviation of the residuals between the observed spectra and their syntheses across the wavelength range of the line list are 8.3×10^{-3} and 2.2×10^{-2} for the Sun and Arcturus respectively.

Table 3
Blue Line List (4100–6300 Å)

Wavelength (Å)	Species[a]	EP[b] (eV)	log *gf*[c]
5183.409	57.1	0.403	−0.6
5183.414	69.1	4.744	−2.65
5183.436	24.1	6.282	−3.172
5183.465	26.0	3.111	−5.06
5183.466	27.0	4.113	−1.187
5183.493	106.00112	3.244	−2.848
5183.506	106.00113	1.569	−3.974
5183.518	607.0	1.085	−4.211
5183.544	26.0	5.064	−3.886
5183.55	58.1	1.706	−2.27
5183.565	106.00112	3.55	−2.811
5183.578	607.0	1.204	−2.653
5183.598	23.1	6.901	−3.568
5183.604	12.0	2.717	−0.167
5183.615	607.0	1.085	−3.003
5183.683	607.0	1.205	−4.499
5183.683	106.00113	1.29	−4.921
5183.686	106.00113	2.371	−3.586
5183.708	40.0	0.633	−1.62
5183.709	22.1	1.892	−2.535
5183.748	58.1	1.482	−1.56
5183.794	106.00112	1.43	−2.866
5183.803	24.0	5.277	−3.52

Notes. The line list presented here is a subset of the entire line list, which spans 4100–6300 Å. The range of wavelengths presented here spans 0.4 Å around the strong Mg I line at 5183.604 Å. The line list is formatted to be compatible with MOOG.
[a] A unique code corresponding to chemical species. For example, 12.0 indicates Mg I, 22.1 indicates Ti II, 106.00112 indicates CN for carbon-12, and 106.0113 indicates CN for carbon-13.
[b] Excitation potential.
[c] Oscillator strength. Transitions modified in the vetting process have fewer than three decimal places.

4.2. Synthetic Spectra

We employ the ATLAS9 (Kurucz 1993) grid of model stellar atmospheres, with no convective overshooting (Castelli et al. 1997). We base our grid on recomputed (Kirby et al. 2009

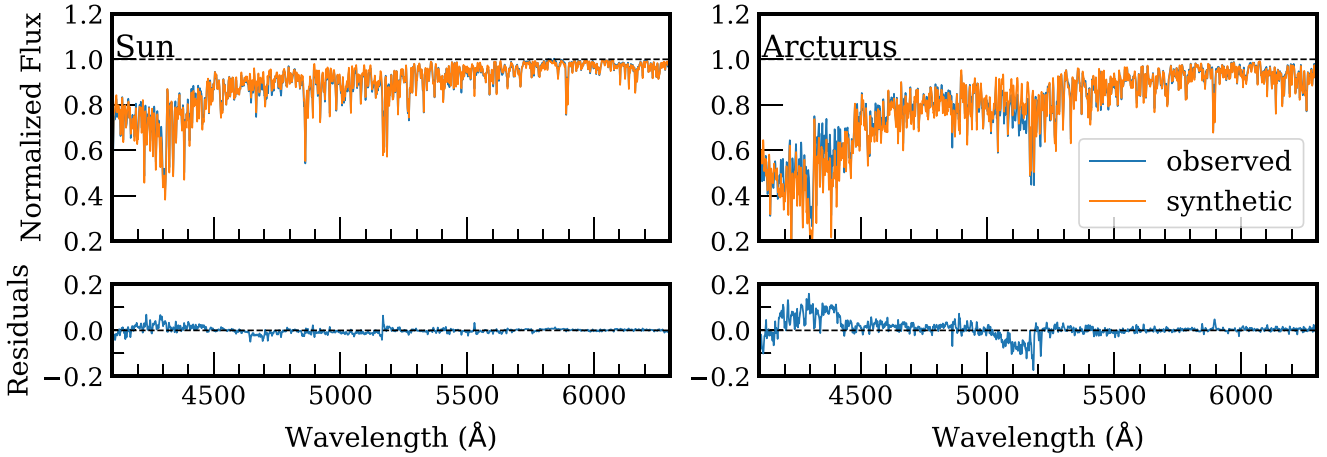

Figure 1. (Top) A comparison between high-resolution spectra (Hinkle et al. 2000; blue) of the Sun (left) and Arcturus (right) and the synthetic spectra (orange) generated using the blue line list (Section 4.1). Both spectra are smoothed to the expected resolution of the DEIMOS 600ZD grating (∼2.8 Å). For a description of synthetic spectrum generation, see Section 4.2. (Bottom) The difference between the observed and synthetic spectra for the Sun and Arcturus. To improve the agreement between the synthetic and observed spectra, we have manually vetted the line list, adjusting the oscillator strengths of discrepant atomic transitions as necessary. In this process, we have favored the Sun over Arcturus, thus the larger residuals between the observed and synthetic spectra for the latter star (which has a lower effective temperature).

and references therein) ATLAS9 model atmospheres with updated opacity distribution functions, available for $[\alpha/\mathrm{Fe}] = 0.0$ and $+0.4$ (Castelli & Kurucz 2003). We adopt the solar composition of Anders & Grevesse (1989), except for Fe (Sneden et al. 1992). The elements considered to be α-elements are O, Ne, Mg, Si, S, Ar, Ca, and Ti.

For stellar parameters between grid points, we linearly interpolated to generate model atmospheres within the ranges $3500\,\mathrm{K} < T_{\rm eff} < 8000\,\mathrm{K}$, $0.0 < \log g < 5.0$, $-4.5 < [\mathrm{Fe/H}] < 0.0$, and $-0.8 < [\alpha/\mathrm{Fe}] < +1.2$. A full description of the grid is presented in Table 4. Here, $[\alpha/\mathrm{Fe}]$ represents the total α-element abundance for the atmosphere, which augments the abundances of individual α-elements without distinguishing between their relative abundances. In total, the grid contains 316,848 synthetic spectra.

We generated the synthetic spectra using MOOG (Sneden 1973), an LTE spectral synthesis software. MOOG takes into account neutral hydrogen collisional line broadening (Barklem et al. 2000; Barklem & Aspelund-Johansson 2005), in addition to radiative and Stark broadening and van der Waals line damping. The most recent version (2017) includes an improved treatment of Rayleigh scattering in the continuum opacity (A. Ji 2019, private communication). The resolution of each generated synthetic spectrum is 0.02 Å.

4.3. Photometric Constraints

To reduce the dimensionality of the parameter space and to optimize our ability to find the global chi-squared minimum in the parameter estimation (Section 4.5), we constrained the effective temperature and surface gravity of the synthetic spectra by available Johnson-Cousins *VI* photometry for red giant stars in our sample. The photometric effective temperature is estimated using a combination of the Padova (Girardi et al. 2002), Victoria-Regina (VandenBerg et al. 2006), and Yonsei-Yale (Demarque et al. 2004) sets of isochrones, assuming an age of 14 Gyr and an α-element abundance of 0.3 dex. If available, we also employed the Ramírez & Meléndez (2005) color temperature. We adopted a single effective temperature ($T_{\rm eff,phot}$) and associated uncertainty ($\sigma_{T_{\rm eff,phot}}$) from an average of the isochrone/color temperatures for each star.

Table 4
Parameter Ranges of Blue Grid (4100–6300 Å)

Parameter	Minimum Value	Maximum Value	Step
$T_{\rm eff}$ (K)	3500	5600	100
	5600	8000	200
$\log g$ (cm s^{-2})	0.0 ($T_{\rm eff} < 7000$ K)	5.0	0.5
	0.5 ($T_{\rm eff} > 7000$ K)	5.0	0.5
[Fe/H]	-4.5[a] ($T_{\rm eff} \leqslant 4100$ K)	0.0	0.1
	-5 ($T_{\rm eff} > 4100$ K)	0.0	0.1
$[\alpha/\mathrm{Fe}]$	-0.8	1.2	0.1

Note.
[a] Below $[\mathrm{Fe/H}] < -4.5$ for $T_{\rm eff} \leqslant 4100$ K, certain stellar atmosphere models fail to converge when solving for molecular equilibrium in each atmospheric layer. Synthetic spectra with $[\mathrm{Fe/H}] < -4.5$ exist for a majority of $T_{\rm eff}$–$\log g$ pairs for $T_{\rm eff} \leqslant 4100$ K, but our grid is complete for all parameter combinations only above $[\mathrm{Fe/H}] = -4.5$ in this regime.

We determined the photometric surface gravity in a similar fashion. However, no color–$\log g$ relation exists, so we could not include this additional source for the photometric surface gravity. Unlike the effective temperature, we did not solve for $\log g$ using spectral synthesis techniques, as the errors on the photometric surface gravity are negligible when the distance is known. Additionally, low- and medium-resolution spectra cannot effectively provide constraints on its value owing to the lack of ionized lines in the spectra. Thus, we held $\log g$ fixed in the abundance determination.

4.4. [Fe/H] and [α/Fe] Regions

In order to increase the sensitivity of the synthetic spectrum fit to a given abundance measurement, we constructed wavelength masks that highlight regions that are particularly responsive to changes in $[\mathrm{Fe/H}]$ and $[\alpha/\mathrm{Fe}]$. We employed the same procedure as Kirby et al. (2009) to make the masks, starting with a base synthetic spectrum for each combination of $T_{\rm eff}$ (3500–8000 K in steps of 500 K) and $\log g$ (0.0–3.5 in steps of 0.5 dex). We assumed a bulk metallicity

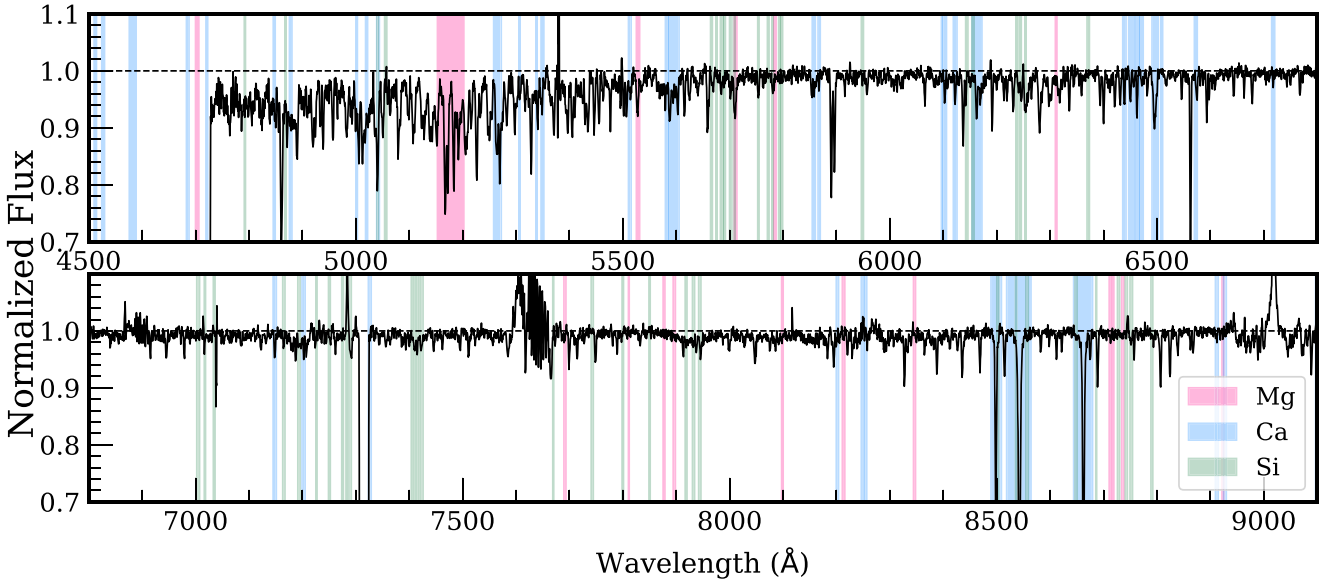

Figure 2. Wavelength regions sensitive to changes in [α/Fe] for the spectral resolution of the DEIMOS 600ZD grating (~2.8 Å). We show an example spectrum (black) over the wavelength range 4500–9100 Å, where we corrected the spectrum for telluric absorption (Section 3.1) and performed an initial continuum normalization (Section 3.3). We do not show spectral regions with wavelengths below 4500 Å, because a low S/N generally prevents utilization of the observed spectrum in this wavelength range. The spectrum is for a star in the GC NGC 2419. Spectral regions sensitive to Mg, Ca, and Si are shown as highlighted ranges in magenta, blue, and green respectively. The atmospheric value of [α/Fe] is measured using the union of the Mg, Ca, and Si spectral regions.

[Fe/H] $= -1.5$ and solar [α/Fe] for the atmosphere. We then generated synthetic spectra with either enhanced or depleted values of individual element abundances (Fe, Mg, Si, Ca, and Ti) for each $T_{\rm eff}$–log g pair and compare to the base synthetic spectra, identifying wavelength regions that differ by more than 0.5%. In the determination of the [Fe/H] and [α/Fe] wavelength regions, we smoothed all synthetic spectra used to an approximation of the expected resolution of the 600ZD grating (~2.8 Å) across the entire spectrum (4100–9100 Å). We then compared the spectral regions for each element against the line list and high-S/N (>100) spectra of cool ($T_{\rm eff} < 4200$ K) GC stars, eliminating any regions that do not have a corresponding transition in the line list or an absorption feature in the spectra.

Although our measurements reflect the atmospheric value of [α/Fe], we constructed the associated wavelength mask from the regions sensitive to changes in the individual elements Mg, Si, and Ca. We excluded Ti from the [α/Fe] mask owing to the prevalence of regions sensitive to Ti at bluer optical wavelengths, such that we cannot meaningfully isolate its elemental abundance. Figure 2 illustrates our [α/Fe] mask across the entire usable spectral range (4500–9100 Å; Section 2). The [Fe/H] spectral regions cover 92% and 51% of the wavelength range in the red and blue, respectively, whereas the [α/Fe] regions span 15% and 12% of the same wavelength ranges. The overlap between the [Fe/H] regions and [α/Fe] regions is 16% and 23% in the blue and red, respectively. We emphasize that [Fe/H] and [α/Fe] are measured separately and iteratively (Section 4.5).

4.5. Parameter Determination from Spectral Synthesis

Here, we outline the steps involved in our measurement of atmospheric parameters and elemental abundances from spectral synthesis of low-resolution spectra. Figure 3 illustrates the final continuum-normalized observed spectrum and best-fit synthetic spectrum, resulting from our measurement procedure for a high S/N RGB star in a MW GC. Our method is nearly identical to that of Kirby et al. (2009), excepting for our introduction of an additional free parameter, $\Delta\lambda$, the resolution of the observed spectrum. We use a Levenberg–Marquardt algorithm to perform each comparison between a given observed spectrum and a synthetic spectrum. We weight the comparison according to the inverse variance of the observed spectrum. In each step, the synthetic spectra utilized in the minimization are interpolated onto the observed wavelength array and smoothed to the fitted observed resolution, $\Delta\lambda$, prior to comparison with a given observed spectrum.

1. $T_{\rm eff}$, *[Fe/H], and* $\Delta\lambda$, *first pass*. All three parameters are allowed to vary simultaneously in the fit. We use only regions sensitive to [Fe/H] (Section 4.4) in this measurement. We choose to measure $\Delta\lambda$ simultaneously with $T_{\rm eff}$ and [Fe/H] to prevent the chi-squared minimizer from under- or oversmoothing the synthetic spectrum to compensate for the initial guesses of $T_{\rm eff}$ and [Fe/H], which are offset from the final parameter values corresponding to the global χ^2 minimum. The [Fe/H] regions cover almost the entire spectrum (92%) in the wavelength range 4100–6300 Å and a majority of the spectrum (51%) in the range 6300–9100 Å, such that using the entire spectrum to measure $\Delta\lambda$ does not change the results within the statistical uncertainties.

   We assume a starting value of $T_{\rm eff,phot}$ (Section 4.3) for the spectroscopic effective temperature. $T_{\rm eff}$ is constrained by photometry using a Gaussian prior, such that χ^2 increases if $T_{\rm eff}$ deviates substantially from $T_{\rm eff,phot}$, as defined by the error associated with the photometric effective temperature ($\sigma_{T_{\rm eff,phot}}$). As motivated in Section 4.3, log g is fixed at the photometric value in all steps. We initialize [Fe/H] at -2 dex, where we performed tests to ensure that the final value of [Fe/H] does not depend on the initial guess. Similar to the approach for $T_{\rm eff}$, we enforce a Gaussian prior with a

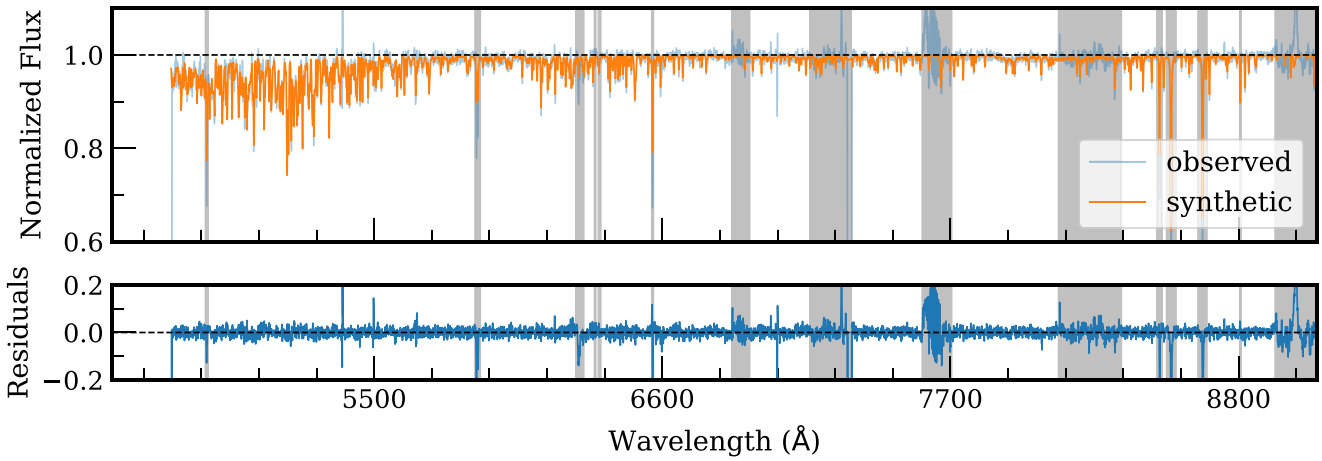

Figure 3. An example of a continuum-normalized observed spectrum (light blue) and its best-fit synthetic spectrum (orange). The observed spectrum corresponds to the same object in Figure 2. We show the the entire fitted wavelength range (∼4500–9100 Å) for this object. The highlighted regions (gray) correspond to our standard mask (Section 3.4), which excludes lines such as Hβ, and Na D1 and D2 from the fit. We adopt the parameters of the best-fit synthetic spectrum for the observed spectrum, $T_{\rm eff} = 4300$ K, log $g = 0.71$ dex, [Fe/H] $= -2.07$ dex, [α/Fe] $= 0.29$ dex, and $\Delta\lambda = 2.60$ Å FWHM. We measure $\chi^2_\nu = 1.63$ for the quality of the fit across the full wavelength range, based on the regions of the spectrum used to measure [Fe/H] (Section 4.4). The normalized residuals (dark blue) between the continuum-refined observed spectrum and best-fit synthetic spectrum are also shown. The residuals have been scaled by the inverse variance of the observed spectrum and the degree of freedom of the fit, such that each pixel represents the direct contribution to χ^2_ν.

mean of 2.8 Å and standard deviation of 0.05 Å on $\Delta\lambda$, according to the expected spectral resolution for the 600ZD grating.[7] For the first iteration of the continuum refinement, [α/Fe] remains fixed at solar. In subsequent iterations, [α/Fe] is fixed at the value determined in step 2. The other parameters are allowed to vary until the best-fit synthetic spectrum is found.

2. *[α/Fe], first pass.* $T_{\rm eff}$, [Fe/H], and $\Delta\lambda$ are fixed at the values determined in step 1 while [α/Fe] is allowed to vary, assuming a starting value of solar for the first iteration of the continuum refinement. Otherwise, the starting value is the value of [α/Fe] determined in the last iteration of the continuum refinement. As in the case of [Fe/H], the final value of [α/Fe] does not depend on the initial guess. In the determination of the best-fit synthetic spectrum, only wavelength ranges sensitive to variations in the α-element abundance are considered (Section 4.4).
3. *Iterative continuum refinement.* After a best-fit synthetic spectrum is determined according to steps 1 and 2, we refine the continuum normalization according to Section 3.3. We perform the continuum refinement iteratively, enforcing the convergence conditions that the difference in parameter values between the previous and current iteration cannot exceed 1 K, 0.001 dex, 0.001 dex, and 0.001 Å for $T_{\rm eff}$, [Fe/H], [α/Fe], and $\Delta\lambda$ respectively. If these conditions are not met in a given iteration, the continuum-refined spectrum is used to repeat steps 1 and 2 until convergence is achieved. If the maximum number of iterations ($N_{\rm iter,max} = 50$) is exceeded, which occurs for a small fraction of observed spectra, we do not include the observed spectra in the subsequent analysis.
4. *[Fe/H], second pass.* [Fe/H] is redetermined, where $T_{\rm eff}$, $\Delta\lambda$, and [α/Fe] are fixed at their converged values from step 3. We use the final continuum-refined observed spectrum determined in step 3 in this step and all remaining steps.
5. *[α/Fe], second and final pass.* We repeat step 2, holding [Fe/H] fixed at the value determined in step 4.
6. *[Fe/H], third and final pass.* We repeat step 4, holding [α/Fe] fixed at the value determined in step 5.

[7] Approximating the spectral resolution by constant value of $\Delta\lambda$ over the full spectrum does not impact the determination of either [Fe/H] or [α/Fe]. Even if $\Delta\lambda$ oversmooths (undersmooths) the spectrum in the fitting procedure, it should not alter the identified χ^2 minimum for [Fe/H] and [α/Fe], given that the effect of oversmoothing (undersmoothing) the core and wings of an absorption feature should effectively negate each other. However, approximating the spectral resolution by $\Delta\lambda$ could increase χ^2_ν, consequently increasing the statistical uncertainties on the abundances.

5. GC Validation Tests

We demonstrate the robustness of our LRS technique by applying it to a set of MW GCs: NGC 2419, NGC 1904 (M79), NGC 6864 (M75), NGC 6341 (M92), and NGC 7078 (M15).

NGC 2419 is a luminous outer halo GC located ∼90 kpc away from the Galactic center (Harris et al. 1997) with multiple stellar populations, but no detected variation in [Fe/H] (Cohen & Kirby 2012). NGC 6864 also exhibits evidence for chemically distinct populations, including a marginal spread in [Fe/H] (∼0.07 dex; Kacharov et al. 2013). It is a relatively young GC (Catelan et al. 2002) at a Galactocentric radius of ∼15 kpc (Harris et al. 1997). NGC 1904 (∼19 kpc; Harris et al. 1997) possesses an extended blue horizontal branch, but it is otherwise a typical cluster. NGC 6341 (∼9 kpc; Harris et al. 1997) is notable primarily for being very metal-poor ([Fe/H] ~ -2.3 dex). NGC 7078 is similarly metal-poor, and has been observed to exhibit variations in α-elements (Sneden et al. 2000; Carretta et al. 2009b). For a summary of observations used in our validation tests, see Table 1.

5.1. Membership

For all subsequent analysis in this section, we utilize only stars that have been identified as RGB or AGB star members by Kirby et al. (2016). Membership is defined using both radial velocity and metallicity criteria based on MRS, such that any star whose measurement uncertainties are greater than 3σ from the mean of either radial velocity or metallicity is not

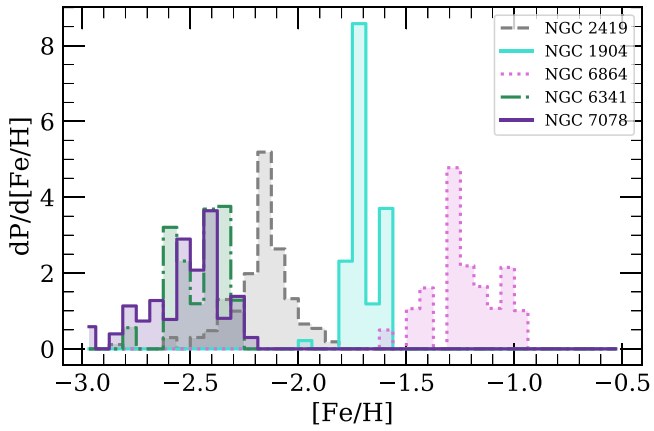

Figure 4. Error-weighted metallicity ([Fe/H]) distribution functions for RGB members of Galactic globular clusters NGC 2419 (gray), NGC 1904 (cyan), NGC 6864 (magenta), NGC 6341 (green), and NGC 7078 (purple). Only stars for which δ[Fe/H] < 0.3 dex are shown. We find mean cluster metallicities of -2.14 dex, -1.70 dex, -1.22 dex, -2.45 dex, and -2.50 dex for the four respective clusters.

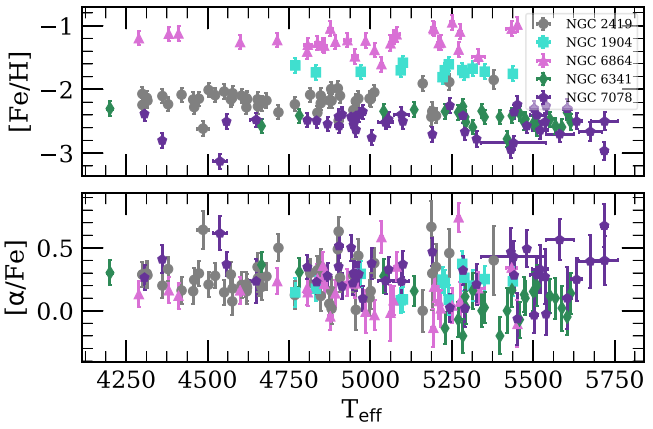

Figure 5. (Top) metallicity ([Fe/H]) and (bottom) [α/Fe] vs. spectroscopic effective temperature ($T_{\rm eff}$). We show only stars with δ[Fe/H] < 0.3 dex and δ [α/Fe] < 0.3 dex in each panel. The lack of a trend between both [Fe/H] and [α/Fe] with respect to $T_{\rm eff}$ for each GC implies that our chemical abundance analysis is robust to systematic covariance in these parameters.

considered a member. The colors and magnitudes of member stars must also conform to the cluster's giant branch.

5.2. Metallicity

As described in Section 4.5, we measure metallicity from spectral regions sensitive to variations in [Fe/H]. In addition to membership criteria (Section 5.1), we further refine our sample by requiring that the 5σ contours in $T_{\rm eff}$, [Fe/H], and [α/Fe] (Section 4.5) identify the minimum. This condition is effectively equivalent to requiring that a given star has sufficient S/N, a converged continuum iteration, and overall high-enough quality fit (χ^2_ν) to produce a reliable abundance measurement.

We illustrate our results for [Fe/H] in the form of metallicity distribution functions (Figure 4) for NGC 2419, NGC 1904, NGC 6864, and NGC 6341, where we weight the distribution according to the total error in [Fe/H]. For a discussion of the measurement uncertainties, including systematic uncertainties, see Section 7. We find that $\langle$[Fe/H]$\rangle = -2.18 \pm 0.15$ dex, -1.70 ± 0.08 dex, -1.23 ± 0.15 dex, -2.45 ± 0.12 dex, and -2.53 ± 0.19 dex for NGC 2419, NGC 1904, NGC 6864, NGC 6341, and NGC 7078 respectively, where $\langle$[Fe/H]$\rangle$ is weighted according to the inverse variance of the total measurement uncertainty. These values approximately agree with the corresponding quantities from HRS: -2.12 ± 0.09 (Cohen & Kirby 2012), -1.58 ± 0.03 (Carretta et al. 2009b), -1.16 ± 0.07 (Kacharov et al. 2013), -2.34 dex (Sneden et al. 2000),[8] and -2.32 ± 0.07 dex, respectively. In particular, we note that we find a spread in [Fe/H] for M15 that is likely not intrinsic (Carretta et al. 2009a), but rather a consequence of measurement uncertainty. Our estimate of the systematic uncertainty in [Fe/H] (Section 7) incorporates this dispersion in [Fe/H] measurements. We present a detailed comparison of our [Fe/H] measurements to HRS abundances in Section 6.

As another example of our ability to reliably recover abundances, we show [Fe/H] and [α/Fe] versus spectroscopically determined $T_{\rm eff}$ in Figure 5 for all GCs. In a nearly monometallic population like a GC, the correlation of metallicity with other fitted parameters, such as $T_{\rm eff}$, would indicate the presence of systematic effects. Because $T_{\rm eff}$ is strongly covariant with [Fe/H], the fitting procedure might erroneously select a lower value of [Fe/H] and $T_{\rm eff}$ in order to match spectral features. Figure 5 presents evidence against any such correlation. The same argument can be extended to the α-element abundance of a GC, given the assumption of chemical homogeneity. Similarly, we do not see any correlation between [α/Fe] and $T_{\rm eff}$.

5.3. α-element Abundance

Similarly, we do not anticipate a correlation between [Fe/H] and [α/Fe] within a GC. [α/Fe] abundance impacts the determination of [Fe/H] via its contribution of H^- opacity to the stellar atmosphere through electron donation. Thus, the abundance of [α/Fe] alters stellar atmospheric structure, requiring a re-evaluation of [Fe/H] in the spectral fitting process. The presence of trends between [α/Fe] with [Fe/H] (e.g., increasing [α/Fe] with decreasing [Fe/H]) within a GC, which we expect to contain no such correlations, would indicate systematic effects in measuring abundances. As summarized in Figure 6, no such systematics are consistently present in our data for each GC. Even in the worst case scenario of M15, a massive, very metal-poor GC with a known α-element variation, any apparent anticorrelation is primarily driven by a few outliers in both [Fe/H] and [α/Fe].

6. Comparison to High-resolution Spectroscopy

6.1. High-resolution Data

Given the variety in approaches of HRS studies of the MW GCs, MW dSphs, and MW halo stars listed in Table 1, we provide a summary of the stellar parameter determination and abundance analysis in each case. For all systems, membership is determined based on radial velocities.

1. *NGC 2419*: Using Keck/HIRES ($R \sim 34{,}000$) spectroscopy, Cohen & Kirby (2012) measured [Fe/H], [Mg/Fe], [Si/Fe], and [Ca/Fe] for 13 RGB stars in NGC 2419. They used MOOG (Sneden 1973) in combination with Castelli & Kurucz (2003) atmospheric models to derive equivalent widths from neutral lines across the

[8] Sneden et al. (2000) did not cite random uncertainties on their abundances. We represent their [Fe/H] and [α/Fe] values (Section 6) as simple means.

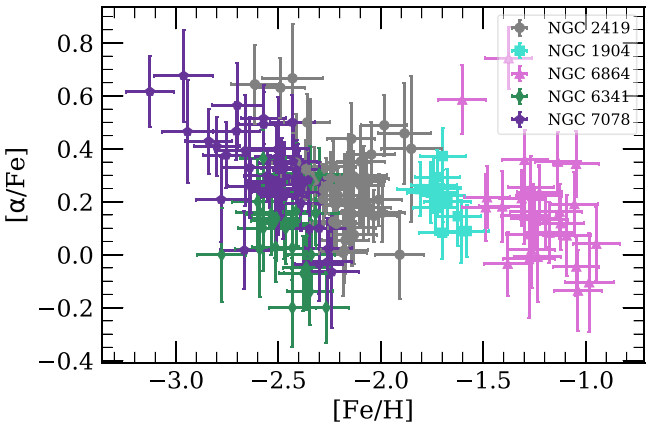

Figure 6. Atmospheric [α/Fe] vs. [Fe/H] for the same data set as Figure 4, where we also exclude points with $\delta([\alpha/\mathrm{Fe}]) > 0.3$ dex. There is no apparent anticorrelation between [α/Fe] and [Fe/H] within a GC, indicating that our method does not show any unphysical covariance between these two parameters.

wavelength range 4500–8350 Å, including the Mg triplet. Stellar parameters were set to photometric values. Measurement uncertainties represent the dispersion of the mean abundance based on the various lines used in the abundance determination.

2. *NGC 6864*: Kacharov et al. (2013) used Magellan/MIKE ($R \sim 30{,}000$) to observe 16 RGB stars in NGC 6864 over a wavelength range of 3340–9150 Å. They measured [Fe/H], [Mg/H], [Si/H], and [Ca/H] via equivalent width measurements using MOOG and Castelli & Kurucz (2003) atmospheric models. Mg was measured from a single line (5711 Å). They determined $T_{\rm eff}$ from excitation equilibrium and surface gravities from $T_{\rm eff}$, extinction-corrected bolometric magnitude ($M_{\rm bol}$), and the known distance to the cluster. The measurement uncertainties are a combination of the random error (based on the number of lines used in the abundance analysis for a given element) and a component that reflects the error from adopted stellar atmosphere parameters. For the latter component, we adopt the larger, more conservative errors that reflect averages based on the entire GC sample of Kacharov et al. (2013).
3. *NGC 1904*: From VLT/UVES ($R \sim 40{,}000$), Carretta et al. (2009b, 2010) performed an abundance analysis based on equivalent width measurements for Fe, Mg, Si, and Ca, respectively, for a sample of 10 RGB stars, over the wavelength range 4800–6800 Å. Following Carretta et al. (2009c), the authors adopted $T_{\rm eff}$ from calibrated $V-K$ colors and surface gravity from $T_{\rm eff}$, $M_{\rm bol}$, and distance moduli, and used Kurucz atmosphere models (with convective overshooting). To determine errors in the stellar atmospheric parameters, Carretta et al. repeated their analysis for each star, varying a single atmospheric parameter each time, to derive an average internal error, in addition to the rms error.
4. *NGC 6341*: Based on WIYN/Hydra ($R \sim 20{,}000$, 5740 Å $< \lambda\lambda <$ 5980 Å) spectra, Sneden et al. (2000) measured [Fe/H], [Si/Fe], and [Ca/Fe] abundances for RGB stars in NGC 6341 and NGC 7078. A single Si transition is used to determine [Si/Fe]. They adopted atmospheric parameters from $B-V$ photometry calibrations and employed MARCS atmosphere models in combination with MOOG. Given that Sneden et al. (2000) did not provide an estimate of abundance errors, we assume an uncertainty of 0.1 dex for all elemental abundances.
5. *NGC 7078*: We utilize a compilation of data from Carretta et al. (2009b, 2010) and Sneden et al. (1997, 2000). The latter two studies employed similar techniques, where Sneden et al. (1997) used a mix of observations from both Hamilton and HIRES. In contrast to the Sneden et al. (2000), Sneden et al. (1997) measured Mg abundances, based on a combination of equivalent width measurements of one to two strong Mg I lines and spectral synthesis of a slightly weaker line. We use [Fe I/H], as opposed to [Fe/H], which is given as the mean of [Fe I/H] and [Fe II/H] and assume 0.1 dex uncertainties on the HRS abundances.
6. *MW dSphs*: For Canes Venatici I (CVnI) and Ursa Minor (UMi), we find a single star in common between each of our DEIMOS slitmasks and the HRS literature (Shetrone et al. 2001; François et al. 2016). François et al. (2016) used VLT/X-shooter spectra ($\lambda = 300$ nm – 1 μm, $R = 7900$–12600) to measure [Fe/H], [Mg/Fe], and [Ca/Fe] for two stars in CVnI. They determined $T_{\rm eff}$ using a color–temperature relation and V, I_C photometry, $\log g$ from $M_{\rm bol}$, and abundances via spectral synthesis using OSMARCS (Gustafsson et al. 1975; Plez et al. 1992) atmosphere models. We estimated the HRS abundance errors based on the typical uncertainties of the published data. Based on Keck/HIRES spectroscopy (4540 Å $\lesssim \lambda\lambda \lesssim$ 7020 Å), Shetrone et al. (2001) measured [Fe/H], [Mg/Fe], and [Ca/Fe] for several stars in UMi, using MOOG and MARCS model atmospheres. They provided large upper limits on [Si/Fe], which we exclude from our analysis. Atmospheric parameters were determined simultaneously and iteratively using dereddened ($B-V$) color–temperature relations, excitation equilibrium, and ionization balance. As for Draco, we use a mixture of data (Shetrone et al. 1998, 2001; Fulbright et al. 2004; Cohen & Huang 2009). The methods of Shetrone et al. (1998) are nearly identical to those of Shetrone et al. (2001), as is the case for Cohen & Huang (2009) in relation to Cohen & Kirby (2012). Aside from using Keck/HIRES spectroscopy and adopting photometric values for atmospheric parameters, the analysis of Fulbright et al. (2004) is similar to that of Fulbright (2000; see discussion of MW halo HRS abundances). Additionally, the majority of Draco stars do not have an HRS measurement of Si abundance.
7. *MW Halo*: We selected five MW halo stars from Fulbright (2000) with $\log g < 3.5$ dex and $[\alpha/\mathrm{Fe}] \lesssim 0.15$ dex or $[\alpha/\mathrm{Fe}] \gtrsim 0.4$ dex. Using high-resolution ($R \sim 50{,}000$), high-S/N Lick/Hamilton spectra, Fulbright (2000) measured Mg, Si, and Ca for 168 halo and disk stars. $T_{\rm eff}$ and $\log g$ were determined iteratively using Fe lines, with initial guesses determined from $V-K$ photometry. Abundances were determined from equivalent width measurements using MOOG and Kurucz model atmospheres with convective overshooting. We use [Fe I/H], as opposed to [Fe/H], which is given as the mean of [Fe I/H] and [Fe II/H]. The abundance errors reflect the rms uncertainty in each elemental abundance.

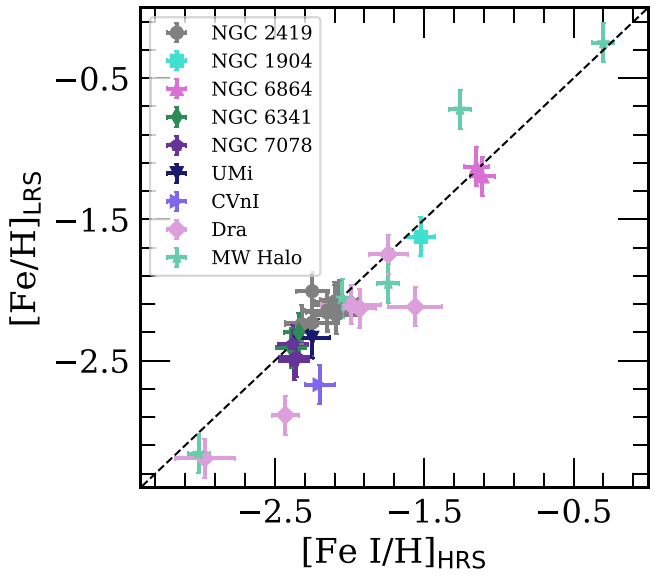

Figure 7. Metallicity measured from LRS ([Fe/H]) vs. HRS ([Fe I/H]) for MW GCs, dSphs, and halo stars. Between the LRS and HRS data sets, we have measurements in common for 30 stars. Although some scatter is present between data sets, $[\mathrm{Fe\,I/H}]_{\mathrm{HRS}}$ and [Fe/H] are strongly correlated at high significance across multiple orders of magnitude in metallicity.

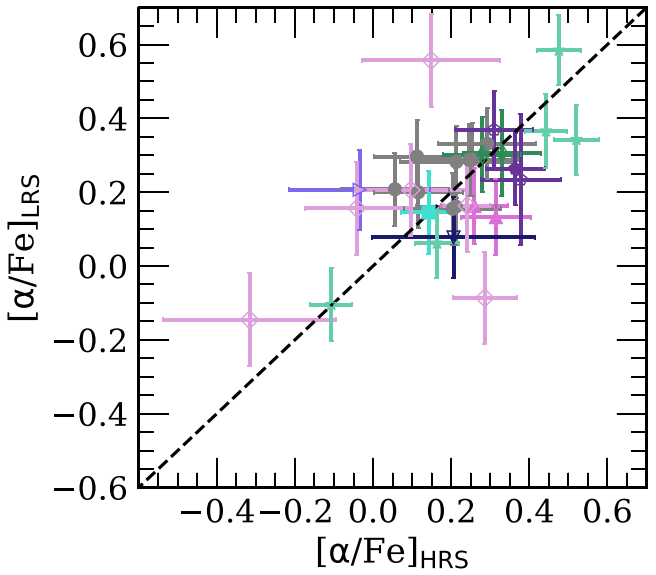

Figure 8. $[\alpha/\mathrm{Fe}]_{\mathrm{HRS}}$ vs. $[\alpha/\mathrm{Fe}]_{\mathrm{LRS}}$ for the same data set as Figure 7. We construct $[\alpha/\mathrm{Fe}]_{\mathrm{HRS}}$ based on a weighting (Section 6.2) of its individual α-element abundances. Unfilled symbols indicate values of $[\alpha/\mathrm{Fe}]_{\mathrm{HRS}}$ constructed from two or fewer individual α-element abundance ratios. The LRS and HRS abundances exhibit broad agreement and show a clear correlation, despite the intrinsic differences between the sets of measurements.

We emphasize that the HRS abundances do not include true estimates of systematic uncertainty, e.g., resulting from limitations from the selected grid of model atmospheres or line list. Additionally, we are comparing our homogeneous LRS abundances to an inhomogeneous HRS sample. As a result, some of the differences among the HRS studies can be attributed simply to different abundance measurement tools and techniques.

6.2. Abundance Comparison

We find good agreement in [Fe/H] for the 30 stars in common between both data sets, where we have included abundance measurements of MW dSphs and MW halo stars, in addition to GCs, to expand our sample size with HRS overlap. In order to perform the comparison, we have shifted the HRS abundances (Anders & Grevesse 1989; Grevesse & Sauval 1998; Gratton et al. 2003; Cohen & Meléndez 2005; Asplund et al. 2009) to the same solar abundance scale as the LRS abundances. Figure 7 shows a strong correlation between the LRS and HRS measurements across a wide metallicity range ($\sim$−3.0–0.0 dex).

In order to compare our $[\alpha/\mathrm{Fe}]$ measurements to an analogous HRS quantity, we construct $[\alpha/\mathrm{Fe}]_{\mathrm{HRS}}$ based on a weighted sum of Mg, Si, and Ca elemental abundances. To derive the weights, we start with a reference synthetic spectrum defined by $T_{\mathrm{eff}} = 4400$ K, $\log g = 1.0$ dex, $[\mathrm{Fe/H}] = -1.8$ dex, which correspond to mean parameter values from HRS studies of NGC 2419, NGC 1904, NGC 6864, and NGC 6341, and $[\alpha/\mathrm{Fe}] = 0$. We assume a spectral resolution of $\Delta\lambda = 2.8$ Å and interpolate the synthetic spectrum onto a wavelength array with spacing equal to the pixel scale of the 600 line mm^{-1} grating ($\sim$0.64 Å). Next, we enhance/deplete the α-element abundance by 0.1, 0.2, and 0.3 dex, calculating the sum of the absolute difference between the reference and enhanced/depleted synthetic spectrum in each case. For each α-element, we utilize only the relevant wavelength regions (Section 4.4) and spectral coverage that corresponds to our data set (4500–9100 Å). Additionally, we exclude contributions from masked wavelength regions (Section 3.4). We adopt the normalized average value of the summed absolute flux differences as our final weight for a given element, i.e.,

$$[\alpha/\mathrm{Fe}]_{\mathrm{HRS}} = 0.282 \times [\mathrm{Mg/Fe}]_{\mathrm{HRS}} + 0.136 \times [\mathrm{Si/Fe}]_{\mathrm{HRS}} + 0.582 \times [\mathrm{Ca/Fe}]_{\mathrm{HRS}}, \quad (1)$$

$$\delta[\alpha/\mathrm{Fe}]_{\mathrm{HRS}} = [(0.282 \times \delta[\mathrm{Mg/Fe}]_{\mathrm{HRS}})^2 + (0.136 \times \delta[\mathrm{Si/Fe}]_{\mathrm{HRS}})^2 + (0.582 \times \delta[\mathrm{Ca/Fe}]_{\mathrm{HRS}})^2]^{1/2}. \quad (2)$$

In Figure 8, we utilize Equations (1) and (2) to directly compare HRS and LRS α-element abundances for the same sample as Figure 7. A clear positive correlation exists between $[\alpha/\mathrm{Fe}]_{\mathrm{LRS}}$ and $[\alpha/\mathrm{Fe}]_{\mathrm{HRS}}$, with some degree of scatter present. We emphasize that $[\alpha/\mathrm{Fe}]_{\mathrm{HRS}}$ represents only an approximation to the atmospheric value of $[\alpha/\mathrm{Fe}]$, given the fundamental differences between the HRS and LRS methods (Section 6.1).

In Table 5, we summarize our findings for $\langle[\alpha/\mathrm{Fe}]\rangle_{\mathrm{LRS}}$ in MW GCs and compare them to equivalent HRS measurements constructed using Equations (1) and (2).[9] In the case of NGC 6341, we construct $[\alpha/\mathrm{Fe}]_{\mathrm{HRS}}$ based only on [Ca/Fe] and [Si/Fe] because Sneden et al. (2000) did not measure [Mg/Fe]. In any instance of an incomplete set of Mg, Ca, and Si abundances for our HRS comparisons, we renormalized the weights in Equations (1) and (2) accordingly. The average LRS α-element abundances are in some cases lower than the HRS measurements by $\sim$0.1 dex, but overlap within the associated standard deviation on the measurement, except for the case of NGC 6341. We find a significantly lower value of

[9] The HRS reference used to construct $[\alpha/\mathrm{Fe}]_{\mathrm{HRS}}$ for NGC 7078 is based on the most recent study of α-enhancement in this cluster. The star-to-star HRS comparisons of Figures 7 and 8 are based on a compilation of values from Sneden et al. (1997, 2000) and Carretta et al. (2009b, 2010) for NGC 7078.

Table 5
$\langle[\alpha/\mathrm{Fe}]\rangle$ in MW GCs

GC	$\langle[\alpha/\mathrm{Fe}]_{\mathrm{LRS}}\rangle$ (dex)	$\langle[\alpha/\mathrm{Fe}]_{\mathrm{HRS}}\rangle$ (dex)
NGC 2419	0.26 ± 0.13	0.21 ± 0.09
NGC 1904	0.20 ± 0.09	0.28 ± 0.02
NGC 6864	0.18 ± 0.18	0.28 ± 0.07
NGC 6341	0.10 ± 0.16	0.37
NGC 7078	0.30 ± 0.15	0.32 ± 0.06

Note. The HRS references for NGC 2419, NGC 1904, NGC 6864, NGC 6341, and NGC 7078 are Cohen & Kirby (2012), Carretta et al. (2009b, 2010), Kacharov et al. (2013), and Sneden et al. (2000). We construct $\langle[\alpha/\mathrm{Fe}]_{\mathrm{HRS}}\rangle$ from a weighting of the available individual HRS α-element abundances (Equation (1)). No published HRS Mg measurements exist for NGC 6341, whereas $\langle[\alpha/\mathrm{Fe}]_{\mathrm{LRS}}\rangle$ includes Mg in all cases.

Table 6
Systematic Uncertainty

Parameter	$\delta_{\mathrm{sys,HRS}}$ (dex)	N_{HRS}[a]	$\delta_{\mathrm{sys,gc}}$[b] (dex)	N_{gc}[c]
[Fe/H]	0.143	29	0.111	154
[α/Fe]	0.039	29	0.094	68

Notes.
[a] Number of stars with both LRS and HRS abundance measurements used to determine the systematic uncertainty from HRS.
[b] The systematic uncertainty as calculated from the intrinsic spread in GCs (Section 7). We adopt these values over the systematic uncertainty determined from the comparison to HRS, $\delta_{\mathrm{sys,HRS}}$ (Section 6.2), given the heterogeneity of the HRS sample (Section 6.1).
[c] Number of stars used to determine the systematic uncertainty from the intrinsic spread in GCs.

$\langle[\alpha/\mathrm{Fe}]\rangle$, although we note that it is particularly difficult to compare between LRS and HRS in this case. Given that NGC 6341 lacks HRS Mg abundances, we cannot perform a meaningful direct comparison of our constructed $\langle[\alpha/\mathrm{Fe}]_{\mathrm{HRS}}\rangle$ to our measurements of $\langle[\alpha/\mathrm{Fe}]_{\mathrm{LRS}}\rangle$, which include Mg.

This apparent offset between the LRS and HRS measurements can be characterized in terms of a systematic uncertainty component. We find that a star-by-star comparison of [α/Fe] and [Fe/H] shows that our LRS results are consistent with those from HRS within the systematic uncertainties (Section 7). We estimate the systematic error by calculating the additional error term that would be required to force the LRS and HRS measurement to agree within one standard deviation. The relevant equation is

$$\frac{1}{N}\sum_{i}^{N}\frac{(\epsilon_{\mathrm{LRS,i}}-\epsilon_{\mathrm{HRS,i}})^2}{(\delta\epsilon^2_{\mathrm{LRS,i}}+\delta\epsilon^2_{\mathrm{HRS,i}}+\delta\epsilon^2_{\mathrm{sys}})}=1, \quad (3)$$

where ϵ represents a given elemental abundance, such as [Fe/H] or [α/Fe], $\delta\epsilon$ is the corresponding statistical uncertainty on the measurement, i is an index representing a given star in common between both the HRS and LRS data sets, and N is the total number of common stars.

For ϵ = [Fe/H] and $N = 30$ stars, we numerically solve Equation (3) to find $\delta\epsilon_{\mathrm{sys}} = 0.176$ dex. A majority of this systematic term is driven by a single MW halo star with a discrepant value of $[\mathrm{Fe/H}]_{\mathrm{LRS}}$. Excluding it from the calculation, we find $\delta\epsilon_{\mathrm{sys}} = 0.143$ dex for $N = 29$ stars. This value is likely more representative of the true systematic uncertainty, given that it is not subject to extreme outliers and exhibits better agreement with an independent calculation of the systematic uncertainty from the intrinsic spread in GCs (Section 7, Table 6). In the case of ϵ = [α/Fe], we find $\delta\epsilon_{\mathrm{sys}} = 0.058$ dex and 0.039 dex, respectively, in the cases of $N = 30$ and $N = 29$. For consistency, we adopt the latter value to reflect the systematic uncertainty in $[\alpha/\mathrm{Fe}]_{\mathrm{LRS}}$ from HRS comparisons. Given the intrinsic heterogeneity of the HRS sample (Section 6.1) and the comparatively limited sample size ($N = 29$ versus $N = 154$), we chose not to adopt these values as our systematic uncertainty. Instead, we favor values calculated from the internal spread in GCs (Section 7).

7. Systematic Uncertainty from the Internal Spread in GCs

The total uncertainty on fitted parameters is composed of two components added in quadrature, the statistical (fit) uncertainty, δ_{fit}, and a systematic component, δ_{sys}. The fit uncertainty is calculated according to the reduced chi-squared value (χ^2_ν) and the diagonals of the covariance matrix of the fit (σ_{ii}), i.e., $\sigma_{ii}(\chi^2_\nu)^{1/2}$. We calculate χ^2_ν using only the regions of the observed spectrum utilized in the fit, e.g., in the case of [Fe/H], we use the wavelength regions sensitive to [Fe/H] (Section 4.4) and not excluded by the pixel mask (Section 3.4). The systematic component encapsulates the uncertainty intrinsic to our method, owing to sources such as the line list (Section 4.1), assumptions involved in spectral synthesis (Section 4.2), details of our method such as the continuum normalization (Section 3.3) and fitting procedure (Section 4.5), and covariance with other fitted parameters.[10]

7.1. Metallicity

Because most GCs, including those in our sample, are nearly monometallic (Carretta et al. 2009a), we can derive an estimate of the systematic uncertainty in [Fe/H], $\delta[\mathrm{Fe/H}]_{\mathrm{sys}}$, by enforcing the condition that the intrinsic dispersion in the GC is zero, i.e.,

$$\sigma^2=\mathrm{var}\left[\frac{[\mathrm{Fe/H}]_i-\langle[\mathrm{Fe/H}]\rangle}{(\delta[\mathrm{Fe/H}]^2_{\mathrm{fit},i}+\delta[\mathrm{Fe/H}]^2_{\mathrm{sys}})^{1/2}}\right]=1, \quad (4)$$

where i is the index for a star in the GC, $\delta[\mathrm{Fe/H}]_{\mathrm{fit}}$ is the S/N-dependent statistical uncertainty in [Fe/H], and $\langle[\mathrm{Fe/H}]\rangle$ is the mean metallicity of the GC, where the mean is weighted by the statistical uncertainty on each measurement of [Fe/H]. Equation (4) follows a reduced chi-squared distribution with an expectation value of unity. Enforcing the condition $\sigma^2 = 1$, we can numerically solve for the most likely value of the systematic uncertainty.

First, we refine our sample by removing outliers in [Fe/H] for each GC. Following Kirby et al. (2016), we calculate the mean metallicity, $\langle[\mathrm{Fe/H}]\rangle$, and standard deviation, $\sigma([\mathrm{Fe/H}])$, for each cluster, and we remove stars that deviate by more than

[10] We do not completely characterize the systematic uncertainty on T_{eff} and $\Delta\lambda$ because our primary goal is to determine abundances. The systematic errors $\delta([\mathrm{Fe/H}])_{\mathrm{sys}}$ and $\delta([\alpha/\mathrm{Fe}])_{\mathrm{sys}}$ already account for errors propagated by inaccuracies in T_{eff} and $\Delta\lambda$. All of the uncertainties in T_{eff} and $\Delta\lambda$ presented in this paper reflect only the statistical uncertainty.

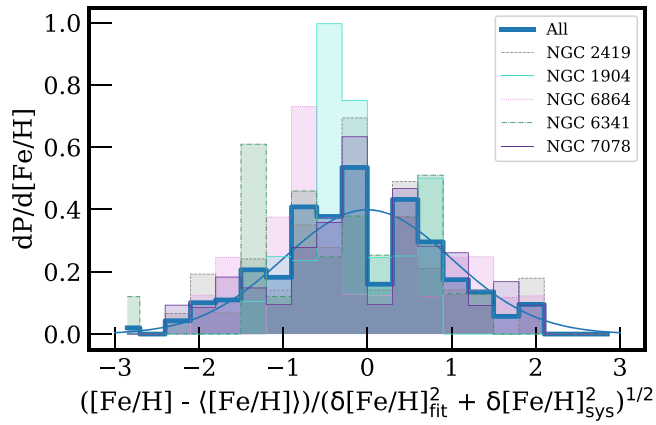

Figure 9. Probability distribution function of [Fe/H] normalized to the mean metallicity of a given cluster ($\langle$[Fe/H]$\rangle$) and weighted by the total error in metallicity. We show the distributions for NGC 2419 (gray), NGC 1904 (cyan), NGC 6864 (magenta), NGC 6341 (green) NGC 7078 purple, and all five clusters (blue; 154 stars). The total error is composed of the statistical uncertainty from the fit (δ[Fe/H]$_{\rm fit}$) and the systematic uncertainty (δ[Fe/H]$_{\rm sys}$). We determine the systematic uncertainty from the intrinsic dispersion in the combined distribution for all three clusters. The Gaussian defined by the systematic uncertainty ($\delta([{\rm Fe/H}]_{\rm sys} = 0.111$ dex) is overplotted.

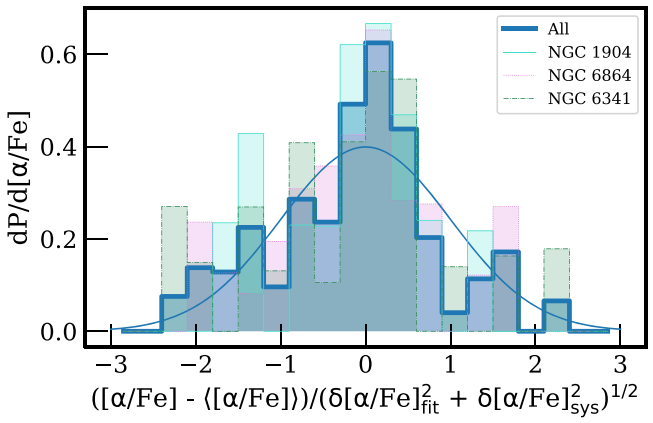

Figure 10. Probability distributions used to determine the systematic uncertainty, as in Figure 9, except for the case of [α/Fe]. We show the distributions for NGC 1904 (cyan), NGC 6864 (magenta), NGC 6341 (green), and all three clusters (blue; 68 stars). We find that $\delta([\alpha/{\rm Fe}]_{\rm sys} = 0.094$ dex. (Section 7.2).

2.58σ (99% confidence level). Then, we recompute $\langle$[Fe/H]$\rangle$ and σ([Fe/H]) from this refined sample, including only stars from the full sample that fulfill the criteria $|[{\rm Fe/H}] - \langle[{\rm Fe/H}]\rangle| - \delta([{\rm Fe/H}]_{\rm fit} < 3\sigma$. The inclusion of $\delta([{\rm Fe/H}]_{\rm fit}$ in the inequality allows stars to be considered members even if they fall outside of the allowed metallicity range, as long as some part of their 1σ confidence intervals falls within the range.

After performing this sigma clipping for each individual cluster, we subtract the mean cluster metallicity from each star's measurement of [Fe/H], and we solve for the intrinsic dispersion based on the combined sample (Equation (4)). We obtain a systematic uncertainty in [Fe/H] of $\delta([{\rm Fe/H}]_{\rm sys} = 0.111$ dex (Table 6) based on 154 stars. We present an illustration of this method in Figure 9, where we show the probability distributions for the total-error-weighted metallicity of each cluster, in addition to the the combined GC sample. The fact that the combined distribution is well approximated by a Gaussian with $\sigma = 1$ indicates that the calculated systematic uncertainty sufficiently accounts for the observed metallicity spread.

Thus, the total error is

$$\delta([{\rm Fe/H}]_{\rm tot} = \sqrt{\delta([{\rm Fe/H}]^2_{\rm fit} + \delta([{\rm Fe/H}]^2_{\rm sys}}. \quad (5)$$

In general, the statistical fit uncertainty for [Fe/H] is negligible compared to the systematic error for GCs. However, this is not be the case for M31, given the low value of the expected S/N.

7.2. α-element Abundance

To determine the systematic uncertainty in [α/Fe], $\delta([\alpha/{\rm Fe}]_{\rm sys}$, we calculate the intrinsic dispersion in the clusters, analogously to Equation (4). Whereas it is generally reasonable to assume that GCs have negligible spread in [Fe/H], the assumption of zero intrinsic variation in [α/Fe] must be evaluated individually for each cluster. For example, abundance analysis of HRS has detected a significant spread in Mg for NGC 2419, where a minority of the population is Mg-abnormal (Cohen et al. 2011; Cohen & Kirby 2012). Large star-to-star variations in Mg have also been found for NGC 7078 from HRS studies (Sneden et al. 2000; Carretta et al. 2009b). Although NGC 6864 possesses chemically distinct populations, O is the only α-element that exhibits significant variation within the cluster, as opposed to Mg, Si, or Ca (Kacharov et al. 2013). NGC 6341 is not known to possess α-element variations (Sneden et al. 2000), with the caveat that no recent Mg abundances from HRS have been published to our knowledge.

We therefore construct our combined GC sample from NGC 1904, NGC 6864, and NGC 6341 to compute $\delta([\alpha/{\rm Fe}]_{\rm sys}$, obtaining a value of 0.094 dex (Table 6) from 68 stars. Figure 10 illustrates that the adopted error floor in [α/Fe] describes the data well. We anticipate a smaller value of $\delta([\alpha/{\rm Fe}]_{\rm sys}$ relative to $\delta([{\rm Fe/H}]_{\rm sys}$, given that the systematic effects (uncertainties in the line list, atmospheric parameters, continuum normalization, etc.) that impact [Fe/H] tend to similarly affect [α/H].

8. The SFH of the Stellar Halo of M31

We apply our spectral synthesis technique to spectra of individual RGB stars in the stellar halo of M31. We select a field with no identified substructure (Gilbert et al. 2007) as an example. We will apply our method to additional M31 stellar halo fields in future work.

8.1. Halo Field Observations

The field, f130_2, is located at 23 kpc in projected radius along the minor axis of M31, and was first observed and characterized by Gilbert et al. (2007) using the Keck II/DEIMOS 1200 line mm^{-1} grating. We selected it owing to its proximity to the 21 kpc halo field of Brown et al. (2007), for which Brown et al. (2009) presented catalogs of deep optical photometry obtained using the Advanced Camera for Surveys (ACS) on the *Hubble Space Telescope*.

Table 7 summarizes our observations of the M31 stellar halo field, which we observed with the same configuration as described in Section 2. The total exposure time was 5.8 hr. Following Cunningham et al. (2016), we designed two separate slitmasks for the single field, with the same mask center, mask position angle, and target list, but with differing slit position

Table 7
M31 Stellar Halo Observations

Object	Date	θ_s ($''$)	$\langle X \rangle$	$t_{\rm exp}$ (s)	N
f130_2a	2018 Jul 19	1.0	1.53	5639	37
f130_2b[a]	2018 Jul 19	1.0	1.16	5758	37
f130_2a	2018 Aug 14	0.86	1.29	4140	37
f130_2a	2018 Oct 10	0.83	1.84	3000	37
f130_2a	2018 Oct 11	0.60	1.49	2400	37

Note.
[a] Slitmasks indicated "a" and "b" are identical, except that the slits are titled according to the median parallactic angle at the approximate time of observation.

angles. Switching slitmasks in the middle of the observation allows us to approximately track the change in parallactic angle over the course of the night. This technique mitigates flux losses due to differential atmospheric refraction (DAR), which disproportionately affects blue wavelengths. Thus, it is especially important to consider DAR when observing with the 600 line mm^1 grating, which covers a wider spectral range than any other DEIMOS grating.

8.2. Sample Selection

The observed field, at a M31 galactocentric radius of 23 kpc, includes a non-negligible contamination fraction of MW foreground dwarf stars. In order to identify M31 members, we used a likelihood-based method (Gilbert et al. 2006) that relies on three criteria to determine membership: the strength of the Na I $\lambda\lambda$8190 absorption line doublet, the (V, I) color–magnitude diagram location, and photometric versus spectroscopic (Ca II $\lambda\lambda$8500) metallicity estimates. Following Gilbert et al. (2007), we excluded radial velocity as a criterion to result in a more complete sample. In total, we identified 37 M31 stellar halo members ($20 \lesssim I_0 \lesssim 22.5$) in this field out of 106 targets.

We required that our abundance measurement technique determine the abundances reliably (Section 5.2): δ([Fe/H]) $<$ 0.5 and $\delta([\alpha/\mathrm{Fe}]) < 0.5$. We also required that the 5σ χ^2 contours in $T_{\rm eff}$, [Fe/H], and [α/Fe] (Section 4.5) identify the minimum. Both of these criteria effectively mimic an S/N cut (S/N $\gtrsim$ 10 Å^{-1}). Lastly, we manually screened member stars for molecular TiO bands between 7055 and 7245 Å (Cenarro et al. 2001; Gilbert et al. 2006), where affected stars exhibit a distinctive pattern. Stars with strong TiO absorption tend to be more metal-rich ([Fe/H] $\gtrsim -1.5$), have red colors ($(V-I)_0 > 2.0$), and can also show unusual χ^2 contours in [α/Fe]. We omitted seven M31 member stars that passed the aforementioned cuts, which meet the $(V-I)_0$ color criterion and show spectral evidence of strong TiO absorption. In total, this reduces the sample size to 11 stars (S/N $\sim$ 10–30 Å^{-1}), for which we present a summary of stellar parameters and chemical abundances in Table 8.

In Figure 11, we show the (I, $V-I$) color–magnitude diagram for all 37 M31 RGB stars in f130_2, highlighting the stars contained in our final sample. No stars in our final sample have $(V-I)_0 > 2.0$, due to the aforementioned exclusion of stars with TiO absorption. Excluding this known color bias, the final sample of RGB stars is well sampled from the full color–magnitude distribution of M31 member stars for this field.

8.3. Kinematics

Given the proximity of our 23 kpc field to the various structures present in the inner halo of M31, we analyzed the kinematics of our finalized 11 star sample relative to that of the broader field. We adopt the heliocentric velocity measurements of Gilbert et al. (2007), which are based on ~1 hr observations obtained with the DEIMOS 1200 line mm^{-1} grating. As discussed in detail by Gilbert et al. (2007), f130_2 contains no detectable substructure and is consistent with the kinematics of a hot stellar halo. Additionally, f130_2 is not a significant contributor to the nearby -300 km s^{-1} kinematically cold component known as the southeast shelf (Fardal et al. 2007; Gilbert et al. 2007). Neither is the field spatially coincident with this feature, given that it is located at a larger minor-axis distance (23 kpc) than its outermost extent in projected radius (18 kpc).

In order to confirm that our final sample is not biased in radial velocity, we present its velocity distribution compared to that of all 37 M31 RGB stars with successful radial velocity measurements in the field in Figure 12. We also show the velocity distribution for 128 M31 RGB stars from the more encompassing field f130 (Gilbert et al. 2007), composed of three distinct slitmasks, including f130_2. Based on a two-sided Kolmogorov–Smirov test, our final sample is consistent at the 99% level with the kinematics of a hot spheroid representing the velocity distribution of f130 ($\bar{v} = -260$ km s^{-1}, $\sigma_v = 132$ km s^{-1}; Gilbert et al. 2007). We identify this kinematic component with the virialized stellar halo of M31.

We also investigate whether f130_2 contains any chemically distinct stellar populations. Figure 13 illustrates the relationship between [Fe/H] and the radial velocity for our final sample. For a more complete representation of these two quantities, we identified stars in f130_2 that possessed well-constrained [Fe/H] measurements (Section 8.2), without enforcing any criteria on the quality of the [α/Fe] measurements. We do not find compelling evidence for correlations between [Fe/H] and radial velocity for f130_2, such that we conclude that there are no kinematically or chemically distinguishable stellar populations within this field. The presence of a tidal feature is not necessary to explain the metallicity or velocity distribution in this field, which is fully consistent with a virialized, phase-mixed stellar population. This conclusion is supported by inspection of the color–magnitude diagram (Figure 11) and the velocity distribution for the broader field (Figure 12).

We acknowledge the possibility that kicked-up M31 disk stars, which are kinematically indistinguishable from halo stars (Dorman et al. 2013), could contribute to f130_2. However, given the distance of f130_2 along the minor axis, it is unlikely that this fraction exceeds ~1% (Dorman et al. 2013). Based on our above kinematic analysis, we can rule out any significant contribution to f130_2 (~100 kpc in the disk plane) from the extended disk of M31 (Ibata et al. 2005; outermost extent ~40–70 kpc in the disk plane). Thus, we conclude that our final sample of 11 M31 RGB stars accurately represents the properties of the smooth stellar halo of M31 in this region.

8.4. Results and Interpretation

Our 11 measurements increase the previous sample size for [α/Fe] measurements in the stellar halo of M31 from four stars (Vargas et al. 2014b). For our field, we find

Table 8
Parameters of 11 M31 RGB Stars

Object	$T_{\rm eff}$[a] (K)	log g (dex)	[Fe/H] (dex)	[α/Fe] (dex)	$\Delta\lambda$[a] (Å)	S/N (Å^{-1})
1282178	4339 ± 7	0.39	−2.4 ± 0.17	0.4 ± 0.32	2.79 ± 0.04	26
1292468	3796 ± 4	0.67	−0.66 ± 0.14	0.52 ± 0.37	2.75 ± 0.03	12
1292496	4368 ± 5	0.7	−0.81 ± 0.14	−0.0 ± 0.27	2.86 ± 0.02	24
1292507	3899 ± 5	0.46	−1.69 ± 0.15	0.61 ± 0.35	2.72 ± 0.05	19
1302682	4075 ± 5	0.85	−1.43 ± 0.14	0.83 ± 0.18	2.79 ± 0.02	19
1302710	4264 ± 9	1.07	−1.64 ± 0.16	0.4 ± 0.4	2.83 ± 0.04	10
1302971	3858 ± 3	0.53	−1.7 ± 0.15	0.75 ± 0.39	2.79 ± 0.04	15
1303039	4144 ± 4	0.52	−2.2 ± 0.15	−0.07 ± 0.25	2.83 ± 0.02	24
1303200	4337 ± 4	0.88	−1.91 ± 0.15	0.07 ± 0.28	2.83 ± 0.02	26
1303382	4356 ± 3	0.78	−2.4 ± 0.15	0.7 ± 0.19	2.79 ± 0.02	30
1303502	3914 ± 3	0.39	−1.2 ± 0.14	0.53 ± 0.15	2.96 ± 0.02	28

Note.
[a] As discussed in Section 7, the errors presented for $T_{\rm eff}$ (and $\Delta\lambda$) represent only the random component of the total uncertainty.

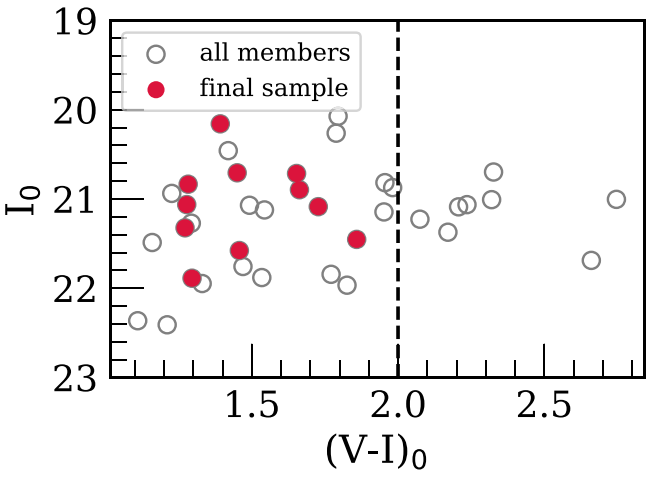

Figure 11. (I, $V-I$) color–magnitude diagram for M31 RGB stars from a 23 kpc field (f130_2) with no identified substructure. We show both stars contained in the final sample (red filled circles; Section 8.2) and the full sample of member stars (gray open circles). The dashed vertical line represents a rough threshold in color above which stars are likely to show evidence for strong TiO absorption in their spectra ($(V-I)_0 > 2.0$). The final sample of stars shows significant overlap with the full distribution of M31 members, aside from the known color biases that we have introduced in our sample selection.

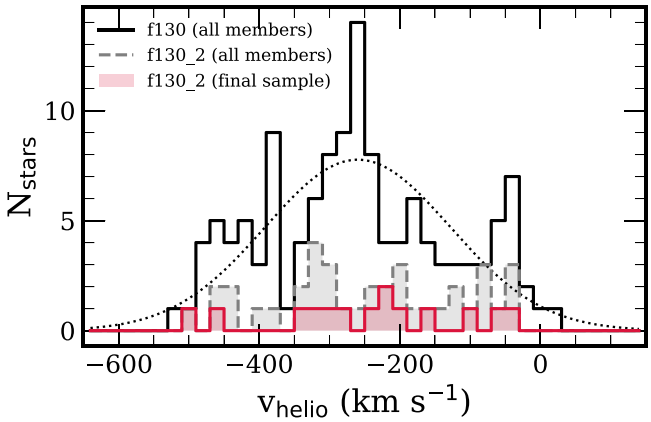

Figure 12. Heliocentric velocity histogram for the final 11 star sample drawn from f130_2 (red) compared to the distributions for all 37 M31 RGB stars in f130_2 (gray) with successful radial velocity measurements. We also show the velocity histogram for 128 M31 RGB stars (black) from the broader sample of nearby fields, including f130_2, known as f130 (Gilbert et al. 2007). The dotted line is the best-fit Gaussian ($\bar{v} = -260$ km s^{-1}, $\sigma_v = 132$ km s^{-1}; Gilbert et al. 2007) to f130, which corresponds to a kinematically hot spheroid component with no detected substructure (i.e., the smooth stellar halo of M31). We find that our final sample is consistent with the kinematics of the hot spheroid.

inverse-variance-weighted values of $\langle$[Fe/H]$\rangle = -1.59$ dex (for a comparison to previous work, see the Appendix), σ([Fe/H]) = 0.56 dex, $\langle[\alpha/\mathrm{Fe}]\rangle = 0.49$ dex, and $\sigma([\alpha/\mathrm{Fe}]) = 0.29$ dex for our uniform, α-enhanced halo field at 23 kpc.

In addition to our 11 measurements of [α/Fe] and [Fe/H], Figure 14 includes the four outer halo stars from Vargas et al. (2014b) for comparison. Vargas et al. (2014b) utilized Gilbert et al.'s (2012) sample of M31 halo stars to identify stars within existing M31 dSph fields (Vargas et al. 2014a) for deeper spectroscopic follow-up. They narrowed their sample by enforcing the criteria that the stars were high-likelihood M31 members with S/N sufficient to measure abundances from MRS (S/N $\gtrsim 15$ Å^{-1}). Their finalized sample originates from the metal-poor outer halo of M31 between ∼70 and 140 kpc. We recompute the inverse-variance-weighted average elemental abundances from their data, finding $\langle$[Fe/H]$\rangle = -1.70$ dex, σ([Fe/H]) = 0.27 dex, $\langle[\alpha/\mathrm{Fe}]\rangle = 0.28$ dex, and $\sigma([\alpha/\mathrm{Fe}]) = 0.22$ dex. In contrast to our work, Vargas et al. (2014b) applied an empirical correction factor to convert between the measured,

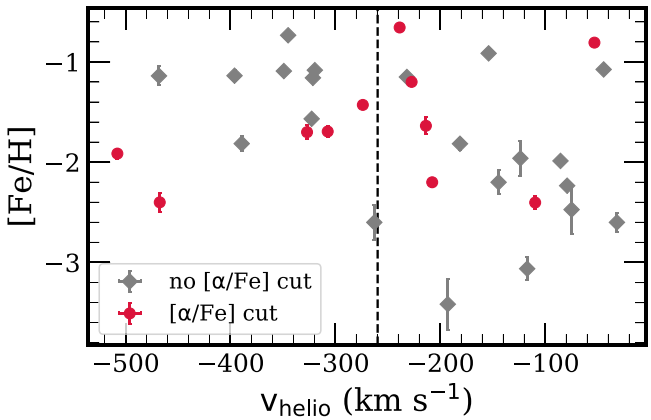

Figure 13. Spectroscopic metallicity ([Fe/H]) as a function of heliocentric velocity for M31 RGB stars in f130_2. The typical uncertainty in velocity (∼3.5 km s^{-1}) is smaller than the size of the data points. In addition to our final sample (red circles), which contains only reliable [α/Fe] measurements (Section 8.2), we show a broader sample (gray diamonds) that contains well-constrained [Fe/H] measurements, with no cuts on [α/Fe]. No apparent correlation exists between radial velocity and metallicity in the field, where our final sample is representative of the broader sample.

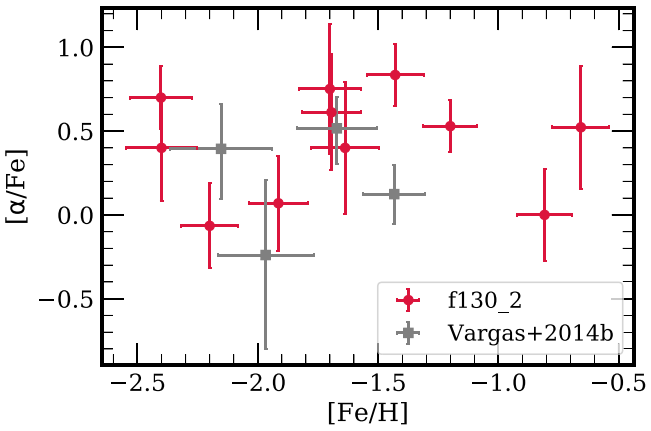

Figure 14. [α/Fe] vs. [Fe/H], measured from LRS, for M31 RGB stars (red circles) in the 23 kpc field. We show a subset of our entire sample, with δ([Fe/H]) < 0.5 dex and δ([α/Fe]) < 0.5 dex, considering only stars with reliable abundance measurements. In total, we present [α/Fe] measurements for 11 M31 halo stars, increasing the previous sample size of four stars (Vargas et al. 2014b). We plot the latter sample of metal-poor halo stars (gray squares; S/N $\gtrsim$ 15 Å^{-1}) over our data set for comparison (S/N $\sim$ 10–30 Å^{-1}).

atmospheric value of [α/Fe] and the average [α/Fe] calculated from individual α-element abundances.

As expected for a smooth halo field, we do not find evidence for a trend of [α/Fe] as a function of [Fe/H], in contrast to the expected abundance pattern (decreasing [α/Fe] with [Fe/H]) for fields dominated by a single, recent accretion event (such as the Giant Southern Stream; Ibata et al. 2001) or dwarf galaxies. Additionally, the fact that our [α/Fe] measurements at 23 kpc are consistent with those at $\sim$70–140 kpc (Figure 14) over the same metallicity range (-2.5 dex $\lesssim$ [Fe/H] $\lesssim -1.5$ dex) suggests the lack of a significant radial trend with [α/Fe] in M31 stellar halo fields absent of substructure. We also find that our 23 kpc field is on average 0.2 dex more metal-rich than the outer halo measurements (Vargas et al. 2014b; see the Appendix for a discussion of potential selection effects). In combination with the approximately constant value of [α/Fe] with both [Fe/H] and radius, this may indicate that we are probing the same extended halo component, which is metal-poor, α-enhanced, and underlies substructure at all radii (Chapman et al. 2006; Gilbert et al. 2012; Ibata et al. 2014).

Given the low luminosity of the smooth halo component ($L \sim 1.9 \times 10^8\, L_\odot$ for [Fe/H]$_{\rm phot} < -1.1$ dex), Ibata et al. (2014) inferred that it would consist of many low-luminosity structures accreted at early times. In terms of SFH, high α-element abundances indicate that the stellar population in f130_2 is characterized by rapid star formation and is dominated by the yields of SNe II. Recognizing that the outer regions ($\gtrsim$20 kpc) of the stellar halo are most likely formed via accretion (Johnston et al. 2008; Cooper et al. 2010; Tissera et al. 2012), we infer that the disrupted dwarf galaxies that were the progenitors of this field likely had short SFHs. Their SFHs could have been truncated by accretion onto M31.

Interestingly, the slightly lower average α-element abundance (0.28 dex) of Vargas et al. (2014b) could suggest that the outer halo is composed of progenitors with more extended chemical evolution as compared to the inner halo. If true, this would be in accordance with expectations from the hierarchical buildup of the stellar halo (Font et al. 2008; Johnston et al. 2008). However, we cannot draw a robust conclusion on this matter given that the average α-element abundances, similar to the case of [Fe/H], between Vargas et al.'s (2014b) sample and our sample are consistent at the 1σ level, which is compounded by limited sample sizes.

Our inferred SFH for f130_2 qualitatively agrees with the trend derived from deep photometry in a nearby *HST*/ACS field located 21 kpc along the minor axis. The mask centers of the fields are separated by 6.33 arcmin on the sky, or 1.44 kpc, assuming a distance to both fields of 783 kpc (Stanek & Garnavich 1998). Using the Brown et al. (2006) method of comparing theoretical isochrones to color–magnitude diagrams, Brown et al. (2007) derived an SFH for the ACS field, assuming [α/Fe] = 0. They found a wide range of stellar ages and metallicities, providing support for an accretion origin, as opposed to early monolithic collapse. The field exhibits evidence for an extended SFH, with the majority of stellar ages between $\sim$8 and 10 Gyr, with a small but non-negligible ($\lesssim$5%) population of stars with ages $\lesssim$8 Gyr. The wide range of metallicity (-2.5 < [Fe/H] < -0.5 dex) that we find in this work is consistent with a multiple-progenitor hypothesis. If the nearby ACS field is representative of f130_2, this implies a composition for f130_2 of intermediate-age system(s) that had elevated star formation rates, quenched at latest $\lesssim$8 Gyr ago.

Comparing our average α-element abundance to that of other systems, we find that, in general, they are similarly α-enhanced. The $\langle$[α/Fe]$\rangle$ for the 23 kpc M31 halo field agrees with that of M31 GCs (0.37 $\pm$ 0.16 dex) within 20 kpc of the galactic center (Colucci et al. 2009). Additionally, the metal-poor MW halo possesses elevated α-element abundance ratios of approximately +0.4 dex (Cayrel et al. 2004; Venn et al. 2004; Ishigaki et al. 2012; Bensby et al. 2014), which is comparable to our result.

Drawing comparisons to M31 dwarf galaxies is less straightforward, given that their average α-element abundance varies from approximately solar to highly α-enhanced ($\sim$0.5 dex; Vargas et al. 2014a). This may indicate a range of star formation timescales for these systems, where some are dominated by old stellar populations ($\gtrsim$10 Gyr ago) and others possess intermediate-age ($\sim$7–10 Gyr ago) stars, although the systematic uncertainties on their SFHs at early times are large (Weisz et al. 2014). Vargas et al. (2014a) also found M31 dwarf galaxies to vary in terms of their internal [α/Fe] versus [Fe/H] abundance patterns, ranging from constant (e.g., And VII; Tollerud et al. 2012) to decreasing [α/Fe] with respect to [Fe/H] (And V; Tollerud et al. 2012). The latter case is in accordance with abundance trends found in MW dwarf spheroidal galaxies (Shetrone et al. 2001, 2003; Tolstoy et al. 2003; Venn et al. 2004; Kirby et al. 2009, 2011a) and systems with more extended SFHs.

In terms of α-enhancement and SFH, our field resembles old M31 dSphs, although it is possible that f130_2 contains intermediate-age stars (Brown et al. 2007). Vargas et al. (2014a) inferred that a present-day stellar halo constructed from M31 dwarf galaxies would be metal-rich, where $\langle$[Fe/H]$\rangle \sim -0.7$ dex (-1.4 dex) for their full sample (old dwarf galaxies only), with a distinct α-element abundance pattern as compared to the MW halo. Given the similarly flat [α/Fe]–[Fe/H] trend between f130_2 and And VII, and the similar $\langle$[Fe/H]$\rangle$ and [Fe/H] range between f130_2 and old M31 dSphs, it is possible that the progenitors of f130_2 were composed of systems similar to And VII. In order to meaningfully test if systems similar to present-day M31 dwarf galaxies could have

contributed to the smooth halo component, or whether the α-element abundance pattern of the smooth halo of M31 differs from that of the MW, we would require larger sample sizes across more halo fields.

9. Summary

In an effort to increase the amount of available high-quality data in M31, we have developed a method of measuring [Fe/H] and [α/Fe] from low-resolution spectroscopy of individual RGB stars. We applied our technique to a field in M31's smooth stellar halo component.

The primary advantages of utilizing low-resolution spectroscopy are (1) the substantial increase in wavelength coverage (from $\sim$2800 Å with MRS to $\sim$4600 Å with LRS) available to constrain the abundances and (2) the accompanying increase in S/N per pixel for the same exposure time and observing conditions. To make the spectral synthesis of DEIMOS LRS a reality, we generated a new grid of synthetic spectra spanning 4100–6300 Å based on a line list we constructed for bluer optical wavelengths. We find the following results:

1. Testing our technique on Galactic GCs, we do not find evidence for any systematic covariance between fitted parameters, such as $T_{\rm eff}$ and [Fe/H]. In light of the the fundamental inhomogeneity of the various HRS samples compared to our LRS data set, our measurements broadly agree with HRS abundances.
2. Based on the intrinsic dispersion in [Fe/H] and [α/Fe] of Galactic GCs with no known abundance variations in Fe, Mg, Ca, or Si, we estimate error floors of $\delta([{\rm Fe/H}])_{\rm sys} = 0.111$ dex and $\delta([\alpha/{\rm Fe}])_{\rm sys} = 0.094$ dex.
3. We present measurements for 11 RGB stars of [Fe/H] and [α/Fe] in the stellar halo of M31, increasing the previous sample size of four stars. The field has no identified substructure and is located at 23 kpc in galactocentric projected radius. We find that $\langle[{\rm Fe/H}]\rangle = -1.59 \pm 0.56$ dex and $\langle[\alpha/{\rm Fe}]\rangle = 0.49 \pm 0.29$ dex for this field.
4. $\langle[\alpha/{\rm Fe}]\rangle$ agrees with the value of the MW halo plateau ($\sim$0.4 dex), M31 GCs, and some α-enhanced M31 dwarf galaxies. Our measurements exhibit overlap with previously published [α/Fe] measurements for M31 halo RGB stars at larger projected radii (70–140 kpc), showing no evidence for a significant radial trend in [α/Fe] in our limited sample.
5. Given its high α-enhancement and low metallicity, we surmise that the smooth halo field is likely composed of disrupted dwarf galaxies with elevated star formation rates and truncated SFHs, accreted early in the formation history of M31.

In future work, we will measure [Fe/H] and [α/Fe] from $\sim$6 hr observations of individual RGB stars in additional M31 halo and tidal stream fields with deep *HST* photometry (Brown et al. 2006), with the goal of deriving chemically based SFHs.

The authors thank the anonymous reviewer for a careful reading of this manuscript and providing thoughtful feedback that improved this paper. We also thank Alis Deason for assistance in line-list vetting, Gina Duggan for useful discussions on generating grids of synthetic spectra, Raja Guha Thakurta for help with observations and insightful conversations, and Luis Vargas and Marla Geha for sharing their data for M31 outer halo RGB stars. I.E. acknowledges support from a Ford Foundation Predoctoral Fellowship and the NSF Graduate Research Fellowship under grant No. DGE-1745301, as well as the NSF under grant No. AST-1614081, along with E.N.K. K.M.G. and J.W. acknowledge support from NSF grant AST-1614569. E.C.C. was supported by an NSF Graduate Research Fellowship as well as NSF grant No. AST-1616540. The analysis pipeline used to reduce the DEIMOS data was developed at UC Berkeley with support from NSF grant AST-0071048.

Appendix
Mean Metallicity: Comparison to Previous Work

In this work, we focus on the determination of [α/Fe] in M31 stellar halo RGB stars. Given the limited sample size of previously existing equivalent measurements, we can only directly compare our [α/Fe] measurements to the Vargas et al. (2014b) sample. However, an extensive body of literature exists on [Fe/H] estimates in the stellar halo of M31, which we discuss in detail here in the context of our measurements.

As presented in Section 8.4, we find $\langle[{\rm Fe/H}]\rangle = -1.59$ dex and $\sigma([{\rm Fe/H}]) = 0.56$ dex for f130_2. In contrast, Brown et al. (2007) estimated $\langle[{\rm Fe/H}]\rangle_{\rm phot} = -0.87$ dex for the nearby ACS field from color–magnitude diagram based SFHs, where their value is more metal-rich than our mean metallicity by 0.71 dex. In terms of both star counts and metallicity, Brown et al. (2007) characterized this field as straddling a transition region between the metal-rich inner halo and the metal-poor outer halo. Although the extended halo ($\gtrsim$60 kpc) is known to be metal-poor based on both photometric and Ca triplet metallicity indicators (Chapman et al. 2006; Guhathakurta et al. 2006; Kalirai et al. 2006; Koch et al. 2008; Gilbert et al. 2014; Ibata et al. 2014), a majority of photometric studies find that the inner halo (20−30 kpc) is as metal-rich as −0.7 dex for fields unpolluted by Giant Southern Stream debris (Guhathakurta et al. 2006; Gilbert et al. 2014). Based on an imaging survey, Ibata et al. (2014) found $[{\rm Fe/H}]_{\rm phot} = -0.7$ dex at 30 kpc for $[\alpha/{\rm Fe}] = 0$, where the mean metallicity does not decline to −1.5 dex until 150 kpc. Assuming $[\alpha/{\rm Fe}] = 0.3$ dex, Kalirai et al. (2006) found $\langle[{\rm Fe/H}]\rangle_{\rm phot} = -1.48$ dex and $\sigma([{\rm Fe/H}]_{\rm phot}) = 0.11$ dex for the extended metal-poor halo ($\gtrsim$60 kpc). They based their measurements on photometry from fields with $\sim$1 hr DEIMOS spectroscopy, but they did not include f130_2 in their analysis of inner halo fields, for which they found $\langle[{\rm Fe/H}]\rangle_{\rm phot} = -0.94$ dex and $\sigma([{\rm Fe/H}]_{\rm phot}) = 0.60$ dex around 30 kpc. Similarly, based on 397 stars between 20 and 40 kpc, Gilbert et al. (2014) found $\langle[{\rm Fe/H}]\rangle_{\rm phot} = -0.70$ dex and $\sigma([{\rm Fe/H}]_{\rm phot}) = 0.53$ dex for $[\alpha/{\rm Fe}] = 0$ in this region (including more metal-rich Giant Southern Stream debris).

Clearly, our value of $\langle[{\rm Fe/H}]\rangle = -1.59$ dex for f130_2 is discrepant with photometric studies of M31's inner halo. This could be a consequence of selection effects against metal-rich stars, given that we discarded stars with strong TiO absorption (Section 8.2). However, we also consider alternative explanations. There are indications that (1) a smooth, metal-poor halo component with no detected substructure is found at all radii, and (2) the photometric metallicities likely overestimate the degree to which the inner halo is metal-rich. Using Ca triplet equivalent width measurements from stacked DEIMOS spectra, Chapman et al. (2006) analyzed major-axis fields (and one minor-axis field) in M31's stellar halo, finding evidence for a

metal-poor stellar halo component ($[Fe/H]_{CaT} = -1.4$ dex) detectable at all radii between 10 and 70 kpc with no apparent metallicity gradient. In an analysis of M31's surface brightness profile, Gilbert et al. (2012) confirmed the detection of this distinct halo component. Additionally, Ibata et al. (2014) found that the smooth halo is ∼0.2 dex more metal-poor than fields dominated by substructure, where metallicities of $-2.5 < [Fe/H] < -1.1$ tend to characterize fields throughout the halo with little to no substructure. In contrast to Kalirai et al. (2006), Koch et al. (2008) analyzed the same DEIMOS fields (including f130_2) using Ca triplet metallicities, finding values systematically more metal-poor in mean metallicity by ∼0.75 dex. The large discrepancy likely results from differences in sample selection and metallicity measurement methodology (photometric versus Ca triplet based).

Whether the methodology employed is photometric, Ca triplet based, or utilizes spectral synthesis can result in substantial differences in metallicity estimates for the same sample (e.g., Lianou et al. 2011). Most relevantly, photometric studies often assume $[\alpha/Fe] = 0$, which can inflate metallicity estimates significantly compared to assuming an α-enhanced field. Using VandenBerg et al. (2006) isochrones, assuming 10 Gyr old stellar populations (Brown et al. 2007), a distance modulus of $(m - M)_0 = 24.63 \pm 0.20$ (Clementini et al. 2011), and $[\alpha/Fe] = 0$ dex, we found $\langle [Fe/H] \rangle_{phot} = -1.40$ dex for our sample of 11 M31 RGB stars. If we instead assume $[\alpha/Fe] = 0.3$, we obtain $\langle [Fe/H] \rangle_{phot} = -1.60$ dex, corresponding to a decrease in the mean photometric metallicity of 0.19 dex. We find nearly identical results by repeating the calculation with a different set of isochrones (Demarque et al. 2004).

The assumptions intrinsic to photometric metallicities, combined with the large amount of tidal debris present in the inner halo of M31 that is included in many previously published measurements in this radial range, are sufficient to explain the large difference between our value of $\langle [Fe/H] \rangle$ for f130_2 and previous analyses in the inner halo of M31. A primary strength of our study is that we can determine both $[\alpha/Fe]$ and $[Fe/H]$ from spectroscopy, without prior assumptions on either parameter. We acknowledge that we may be preferentially sampling brighter, more metal-poor stars in this field, given that we are S/N limited and select against stars with strong TiO absorption. However, given that we can measure both $[Fe/H]$ and $[\alpha/Fe]$ reliably from some of the highest quality spectra in M31's halo yet obtained, we conclude that $\langle [Fe/H] \rangle = -1.59$ dex is likely an accurate representation of our final sample's mean metallicity. Thus, it is possible that our sample in f130_2 represents the metal-poor halo that underlies substructure (Chapman et al. 2006; Gilbert et al. 2014; Ibata et al. 2014) in the inner halo of M31.

ORCID iDs

Ivanna Escala https://orcid.org/0000-0002-9933-9551
Evan N. Kirby https://orcid.org/0000-0001-6196-5162
Karoline M. Gilbert https://orcid.org/0000-0003-0394-8377
Emily C. Cunningham https://orcid.org/0000-0002-6993-0826

References

Anders, E., & Grevesse, N. 1989, GeCoA, 53, 197
Asplund, M., Grevesse, N., Sauval, A. J., & Scott, P. 2009, ARA&A, 47, 481
Barklem, P. S., & Aspelund-Johansson, J. 2005, A&A, 435, 373
Barklem, P. S., Piskunov, N., & O'mara, B. J. 2000, A&AS, 142, 467
Bensby, T., Feltzing, S., & Oey, M. S. 2014, A&A, 562, A71
Brown, T. M., Smith, E., Ferguson, H. C., et al. 2006, ApJ, 652, 323
Brown, T. M., Smith, E., Ferguson, H. C., et al. 2007, ApJL, 658, L95
Brown, T. M., Smith, E., Ferguson, H. C., et al. 2009, ApJS, 184, 152
Carretta, E., Bragaglia, A., Gratton, R., et al. 2010, ApJL, 712, L21
Carretta, E., Bragaglia, A., Gratton, R., D'Orazi, V., & Lucatello, S. 2009a, A&A, 508, 695
Carretta, E., Bragaglia, A., Gratton, R., & Lucatello, S. 2009b, A&A, 505, 139
Carretta, E., Bragaglia, A., Gratton, R. G., et al. 2009c, A&A, 505, 117
Castelli, F., Gratton, R. G., & Kurucz, R. L. 1997, A&A, 318, 841
Castelli, F., & Kurucz, R. L. 2003, in IAU Symp. 210, Modelling of Stellar Atmospheres, Poster Contributions, ed. N. Piskunov, W. W. Weiss, & D. F. Gray (San Francisco, CA: ASP), A20
Catelan, M., Borissova, J., Ferraro, F. R., et al. 2002, AJ, 124, 364
Cayrel, R., Depagne, E., Spite, M., et al. 2004, A&A, 416, 1117
Cenarro, A. J., Cardiel, N., Gorgas, J., et al. 2001, MNRAS, 326, 959
Chapman, S. C., Ibata, R., Lewis, G. F., et al. 2006, ApJ, 653, 255
Clementini, G., Contreras Ramos, R., Federici, L., et al. 2011, ApJ, 743, 19
Cohen, J. G., & Huang, W. 2009, ApJ, 701, 1053
Cohen, J. G., Huang, W., & Kirby, E. N. 2011, ApJ, 740, 60
Cohen, J. G., & Kirby, E. N. 2012, ApJ, 760, 86
Cohen, J. G., & Meléndez, J. 2005, AJ, 129, 303
Colucci, J. E., Bernstein, R. A., Cameron, S., McWilliam, A., & Cohen, J. G. 2009, ApJ, 704, 385
Cooper, A. P., Cole, S., Frenk, C. S., et al. 2010, MNRAS, 406, 744
Cooper, M. C., Newman, J. A., Davis, M., Finkbeiner, D. P., & Gerke, B. F. 2012, spec2d: DEEP2 DEIMOS Spectral Pipeline, Astrophysics Source Code Library, ascl:1203.003
Cunningham, E. C., Deason, A. J., Guhathakurta, P., et al. 2016, ApJ, 820, 18
Demarque, P., Woo, J.-H., Kim, Y.-C., & Yi, S. K. 2004, ApJS, 155, 667
Dorman, C. E., Widrow, L. M., Guhathakurta, P., et al. 2013, ApJ, 779, 103
Faber, S. M., Phillips, A. C., Kibrick, R. I., et al. 2003, Proc. SPIE, 4841, 1657
Fardal, M. A., Guhathakurta, P., Babul, A., & McConnachie, A. W. 2007, MNRAS, 380, 15
Font, A. S., Johnston, K. V., Ferguson, A. M. N., et al. 2008, ApJ, 673, 215
François, P., Monaco, L., Bonifacio, P., et al. 2016, A&A, 588, A7
Fuhr, J. R., & Wiese, W. L. 2006, JPCRD, 35, 1669
Fulbright, J. P. 2000, AJ, 120, 1841
Fulbright, J. P., Rich, R. M., & Castro, S. 2004, ApJ, 612, 447
Gilbert, K. M., Fardal, M., Kalirai, J. S., et al. 2007, ApJ, 668, 245
Gilbert, K. M., Guhathakurta, P., Beaton, R. L., et al. 2012, ApJ, 760, 76
Gilbert, K. M., Guhathakurta, P., Kalirai, J. S., et al. 2006, ApJ, 652, 1188
Gilbert, K. M., Kalirai, J. S., Guhathakurta, P., et al. 2014, ApJ, 796, 76
Gilmore, G., & Wyse, R. F. G. 1998, AJ, 116, 748
Girardi, L., Bertelli, G., Bressan, A., et al. 2002, A&A, 391, 195
Gratton, R. G., Carretta, E., Claudi, R., Lucatello, S., & Barbieri, M. 2003, A&A, 404, 187
Grevesse, N., & Sauval, A. J. 1998, SSRv, 85, 161
Guhathakurta, P., Rich, R. M., Reitzel, D. B., et al. 2006, AJ, 131, 2497
Gustafsson, B., Bell, R. A., Eriksson, K., & Nordlund, A. 1975, A&A, 500, 67
Harris, W. E., Bell, R. A., Vandenberg, D. A., et al. 1997, AJ, 114, 1030
Hinkle, K., Wallace, L., Valenti, J., & Harmer, D. 2000, Visible and Near Infrared Atlas of the Arcturus Spectrum 3727–9300 A (San Francisco, CA: ASP)
Ho, N., Geha, M., Tollerud, E. J., et al. 2015, ApJ, 798, 77
Ibata, R., Chapman, S., Ferguson, A. M. N., et al. 2005, ApJ, 634, 287
Ibata, R., Irwin, M., Lewis, G., Ferguson, A. M. N., & Tanvir, N. 2001, Natur, 412, 49
Ibata, R. A., Lewis, G. F., McConnachie, A. W., et al. 2014, ApJ, 780, 128
Ishigaki, M. N., Chiba, M., & Aoki, W. 2012, ApJ, 753, 64
Johnston, K. V., Bullock, J. S., Sharma, S., et al. 2008, ApJ, 689, 936
Kacharov, N., Koch, A., & McWilliam, A. 2013, A&A, 554, A81
Kalirai, J. S., Gilbert, K. M., Guhathakurta, P., et al. 2006, ApJ, 648, 389
Kalirai, J. S., Zucker, D. B., Guhathakurta, P., et al. 2009, ApJ, 705, 1043
Kirby, E. N., & Cohen, J. G. 2012, AJ, 144, 168
Kirby, E. N., Cohen, J. G., Guhathakurta, P., et al. 2013, ApJ, 779, 102
Kirby, E. N., Cohen, J. G., Smith, G. H., et al. 2011a, ApJ, 727, 79
Kirby, E. N., Guhathakurta, P., Bolte, M., Sneden, C., & Geha, M. C. 2009, ApJ, 705, 328
Kirby, E. N., Guhathakurta, P., Simon, J. D., et al. 2010, ApJS, 191, 352
Kirby, E. N., Guhathakurta, P., & Sneden, C. 2008a, ApJ, 682, 1217
Kirby, E. N., Guhathakurta, P., Zhang, A. J., et al. 2016, ApJ, 819, 135
Kirby, E. N., Lanfranchi, G. A., Simon, J. D., Cohen, J. G., & Guhathakurta, P. 2011b, ApJ, 727, 78
Kirby, E. N., Simon, J. D., Geha, M., Guhathakurta, P., & Frebel, A. 2008b, ApJL, 685, L43
Koch, A., Rich, R. M., Reitzel, D. B., et al. 2008, ApJ, 689, 958

Kramida, A., Ralchenko, Y., Reader, J. & NIST ADS Team 2016, NIST Atomic Spectra Database (version 5.4)
Kupka, F., Piskunov, N., Ryabchikova, T. A., Stempels, H. C., & Weiss, W. W. 1999, A&AS, 138, 119
Kurucz, R. L. 1992, RMxAA, 23, 45
Kurucz, R. L. 1993, PhST, 47, 110
Lanfranchi, G. A., & Matteucci, F. 2003, MNRAS, 345, 71
Lanfranchi, G. A., & Matteucci, F. 2007, A&A, 468, 927
Lanfranchi, G. A., & Matteucci, F. 2010, A&A, 512, A85
Lanfranchi, G. A., Matteucci, F., & Cescutti, G. 2006, A&A, 453, 67
Lianou, S., Grebel, E. K., & Koch, A. 2011, A&A, 531, A152
Newman, J. A., Cooper, M. C., Davis, M., et al. 2013, ApJS, 208, 5
Peterson, R. C., Dalle Ore, C. M., & Kurucz, R. L. 1993, ApJ, 404, 333
Plez, B., Brett, J. M., & Nordlund, A. 1992, A&A, 256, 551
Ramírez, I., & Meléndez, J. 2005, ApJ, 626, 465
Richardson, J. C., Ferguson, A. M. N., Mackey, A. D., et al. 2009, MNRAS, 396, 1842
Shetrone, M., Venn, K. A., Tolstoy, E., et al. 2003, AJ, 125, 684
Shetrone, M. D., Bolte, M., & Stetson, P. B. 1998, AJ, 115, 1888
Shetrone, M. D., Côté, P., & Sargent, W. L. W. 2001, ApJ, 548, 592
Shetrone, M. D., Siegel, M. H., Cook, D. O., & Bosler, T. 2009, AJ, 137, 62
Simon, J. D., & Geha, M. 2007, ApJ, 670, 313
Sneden, C., Kraft, R. P., Prosser, C. F., & Langer, G. E. 1992, AJ, 104, 2121
Sneden, C., Kraft, R. P., Shetrone, M. D., et al. 1997, A&A, 114, 1964
Sneden, C., Pilachowski, C. A., & Kraft, R. P. 2000, AJ, 120, 1351
Sneden, C. A. 1973, PhD thesis, The Univ. Texas
Stanek, K. Z., & Garnavich, P. M. 1998, ApJL, 503, L131
Tanaka, M., Chiba, M., Komiyama, Y., et al. 2010, ApJ, 708, 1168
Tissera, P. B., White, S. D. M., & Scannapieco, C. 2012, MNRAS, 420, 255
Tollerud, E. J., Beaton, R. L., Geha, M. C., et al. 2012, ApJ, 752, 45
Tolstoy, E., Venn, K. A., Shetrone, M., et al. 2003, AJ, 125, 707
VandenBerg, D. A., Bergbusch, P. A., & Dowler, P. D. 2006, ApJS, 162, 375
Vargas, L. C., Geha, M. C., & Tollerud, E. J. 2014a, ApJ, 790, 73
Vargas, L. C., Gilbert, K. M., Geha, M., et al. 2014b, ApJL, 797, L2
Venn, K. A., Irwin, M., Shetrone, M. D., et al. 2004, AJ, 128, 1177
Weisz, D. R., Dolphin, A. E., Skillman, E. D., et al. 2014, ApJ, 789, 147